HEAT TRANSFER OF NANOFLUIDS – BOOM OR BUST

T. McKrell*[a], J. Buongiorno[a], and Lin-wen Hu[b]
*Author for correspondence
[a]Department of Nuclear Science and Engineering,
[b]Nuclear Reactor Laboratory,
Massachusetts Institute of Technology,
Cambridge, Ma,
USA,
E-mail: tmckrell@mit.edu

ABSTRACT

Significant controversy over reports of extraordinary heat transfer in nanofluids has existed. The results of work performed by our group to help resolve some of these issues will be discussed. Heat transfer in fluids is complex and includes phenomena such as conduction (thermal conductivity), convection (laminar and turbulent), and boiling. The results of tests performed with custom experimental apparatuses, including transient hot wire, pool boiling, quench, flow loops, and high-speed infrared (IR) thermography and digital imaging, will be discussed. Additionally, single phase pressure drop measurements for nanofluids will be presented. It will be shown that the effect of nanofluids on pressure drop and conductive and convective heat transfer can be explained by existing theories, if a nanofluid's thermophysical properties are used. However, the enhancement of boiling heat transfer, particularly critical heat flux and quenching, is more challenging to interpret using existing theory because of surface effects. Accordingly, the insights gained from measurements of contact angle, IR imaging, and morphological data will be presented.

INTRODUCTION

Engineered suspensions of nanoparticles in liquids, known recently as 'nanofluids', have generated considerable interest for their potential to enhance the heat transfer rate in engineering systems, while reducing, or possibly eliminating, the issues of erosion, sedimentation and clogging that plagued earlier solid-liquid mixtures with larger particles. According to SciFinder Scholar, in 2008 alone 189 nanofluid-related publications (journal articles and patents) appeared (see Figure 1), and it is estimated that more than 300 research groups and companies are engaged in nanofluids research worldwide. Furthermore, several review papers on nanofluid heat transfer have been published [1, 2, 3, 4, 5, 6, 7] and recently even a book entirely dedicated to nanofluids has been released [8]. In spite of the attention received by this field, uncertainties concerning the fundamental effects of nanoparticles on thermo-physical properties of solvent media remain.

Significant controversy over reports of extraordinary heat transfer in nanofluids has existed. This paper will present the results of our group's work on the effect of nanofluids on heat transfer, work that has focused primarily on helping to resolve these issues. The general headings of thermal conductivity, convection, and boiling have been used here to organize the findings. The thermal conductivity work is best summarized by an international benchmark study that employed laboratories throughout the world to make thermal conductivity measurements on "semi-blind" samples [9]. The convection work included laminar and turbulent forced convection studies [10, and 11]. The increased viscosity of nanofluids with significant loadings is of concern in applying these fluids in engineering systems. Accordingly, these studies also measured the pressure drop associated with the nanofluids. The boiling work that the group has performed includes pool boiling and flow boiling investigations [12, 13, 14, and 81]. This work has focused on the enhanced critical heat flux (CHF) and quenching kinetics that nanofluids provide.
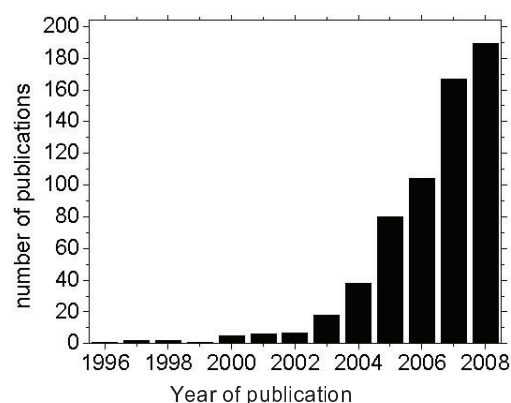
Figure 1 Number of publications containing the term "nanofluid" according to SciFinder Scholar.

1. THERMAL CONDUCTION

1.1. Introduction

Thermal conductivity is the property that has catalyzed the attention of the nanofluids research community the most. As dispersions of solid particles in a continuous liquid matrix, nanofluids are expected to have a thermal conductivity that obeys the effective medium theory developed by Maxwell over 100 years ago [15]. Maxwell's model for spherical and well-dispersed particles culminates in a simple equation giving the ratio of the nanofluid thermal conductivity (k) to the thermal conductivity of the basefluid (k_f):

$$\frac{k}{k_f} = \frac{k_p + 2k_f + 2\phi(k_p - k_f)}{k_p + 2k_f - \phi(k_p - k_f)}$$

Equation 1

where k_p is the particle thermal conductivity and ϕ is the particle volumetric fraction. Note that the model predicts no explicit dependence of the nanofluid thermal conductivity on the particle size or temperature. Also, in the limit of $k_p \gg k_f$ and $\phi \ll 1$, the dependence on particle loading is expected to be

$$\frac{k}{k_f} \approx 1 + 3\phi$$

linear, as given by . However, several deviations from the predictions of Maxwell's model have been reported, including:

- A strong thermal conductivity enhancement beyond that predicted by Eq. (1) with a non-linear dependence on particle loading [16, 17, 18, 19, 20, 21, and 22]
- A dependence of the thermal conductivity enhancement on particle size and shape [21, 23, 24, 25, 26, 27, 28, 29, and 30]
- A dependence of the thermal conductivity enhancement on fluid temperature [26, 31, 32, and 33]

To explain these unexpected and intriguing findings, several hypotheses were recently formulated. For example, it was proposed that:

- Particle Brownian motion agitates the fluid, thus creating a micro-convection effect that increases energy transport [34, 35, 36, 37, and 38]
- Clusters or agglomerates of particles form within the nanofluid, and heat percolates preferentially along such clusters [39, 40, 41, 42, 43, and 44]
- Basefluid molecules form a highly-ordered high-thermal-conductivity layer around the particles, thus augmenting the effective volumetric fraction of the particles [39, 43, 45, and 46].

Experimental confirmation of these mechanisms has been weak; some mechanisms have been openly questioned. For example, the micro-convection hypothesis has been shown to yield predictions in conflict with the experimental evidence [30, 43]. In addition to theoretical inconsistencies, the nanofluid thermal conductivity data are sparse and inconsistent, possibly due to (i) the broad range of experimental approaches that have been implemented to measure nanofluid thermal conductivity (e.g., transient hot wire, steady-state heated plates, oscillating temperature, thermal lensing), (ii) the often-incomplete characterization of the nanofluid samples used in those measurements, and (iii) the differences in the synthesis processes used to prepare those samples, even for nominally similar nanofluids. In summary, the possibility of very large thermal conductivity enhancement in nanofluids beyond Maxwell's prediction and the associated physical mechanisms are still a hotly debated topic.

At the first scientific conference centered on nanofluids (Nanofluids: Fundamentals and Applications, September 16-20, 2007, Copper Mountain, Colorado), it was decided to launch an international nanofluid property benchmark exercise (INPBE), to resolve the inconsistencies in the database and help advance the debate on nanofluid properties.

1.2. Methodology

The exercise's main objective was to compare thermal conductivity data obtained by different organizations for the same samples. Four sets of test nanofluids were procured. To minimize spurious effects due to nanofluid preparation and handling, all participating organizations were given identical samples from these sets, and were asked to adhere to the same sample handling protocol. The exercise was 'semi-blind', as only minimal information about the samples was given to the participants at the time of sample shipment. The minimum requirement to participate in the exercise was to measure and report the thermal conductivity of at least one test nanofluid at room temperature. The data were then reported in a standardized form to the exercise coordinator at the Massachusetts Institute of Technology (MIT) and posted, unedited, at the INPBE website (http://mit.edu/nse/nanofluids/benchmark/index.html). The complete list of 32 international organizations that participated in INPBE, along with the data they contributed, is reported in [9]. INPBE climaxed in a workshop, held on January 29-30 2009 in Beverly Hills, California, where the results were presented and discussed by the participants. The workshop presentations can also be found at the INPBE website, and paper detailing the study in more detail has been written [9].

To strengthen the generality of the INPBE results, it was desirable to select test nanofluids with a broad diversity of parameters; for example, we wanted to explore aqueous and non-aqueous basefluids, metallic and oxide particles, near-spherical and elongated particles, and high and low particle loadings. Also, given the large number of participating organizations, the test nanofluids had to be available in large quantities (> 2 L) and at reasonably low cost.

Accordingly, four sets of test samples were procured. The providers were Sasol (Set 1), DSO National Labs (Set 2), W. R. Grace & Co. (Set 3) and the University of Puerto Rico at Mayaguez (Set 4). The providers reported information regarding the particle materials, particle size and concentration,

basefluid material, the additives/stabilizers used in the synthesis of the nanofluid, and the material safety data sheets. Said information was independently verified, to the extent possible, by the INPBE coordinators (MIT and Illinois Institute of Technology, IIT). Identical samples were shipped to all participating organizations.

Set 1

The samples in Set 1 were supplied by Sasol. These samples were:

- Alumina nanorods in de-ionized water
- De-ionized water. (basefluid sample)
- Alumina nanoparticles (first concentration) in Polyalphaolefins lubricant (PAO) + surfactant
- Alumina nanoparticles (second concentration) in PAO + surfactant
- Alumina nanorods (first concentration) in PAO + surfactant
- Alumina nanorods (second concentration) in PAO + surfactant
- PAO + surfactant. (basefluid sample)

Set 2

The samples in Set 2 were supplied by Dr. Lim Geok Kieng of DSO National Laboratories in Singapore. These samples were:

- Gold nanoparticles in de-ionized water and trisodium citrate stabilizer.
- De-ionized water + sodium citrate stabilizer. (basefluid sample)

Set 3

Set 3 consisted of a single sample, supplied by W. R. Grace & Co.:

- Silica monodispersed spherical nanoparticles and stabilizer in de-ionized water

Set 4

The samples in Set 4 were supplied by Dr. Jorge Gustavo Gutierrez of the University of Puerto Rico – Mayaguez (UPRM). A chemical co-precipitation method was used to synthesize the particles. The Set 4 samples were:

- Mn-Zn ferrite ($Mn_{1/2}$-$Zn_{1/2}$-$Fe2O4$) particles in solution of stabilizer and water.
- Solution of stabilizer (25 wt%) and water (75 wt%). (basefluid sample).

1.3. Results

The thermal conductivity data generated by the participating organizations are shown in Table 1. A very thorough treatment of the data was conducted and is discussed in Reference [9]. It can be seen that for all water-based samples in all four sets most organizations report values of the thermal conductivity that are within ±5% of the sample average. For the PAO-based samples the spread is a little wider, with most organizations reporting values that are within ±10% of the sample average. A note of caution is in order: while all data reported here are nominally for room temperature, what constitutes 'room temperature' varies from organization to organization. In the data analysis only the measurements conducted in the range of 20 – 30 °C were considered. Over this range of temperatures,

the thermal conductivity of the test fluids is expected to vary minimally; for example, water thermal conductivity varies by less than 2.5%.

The thermal conductivity 'enhancement' for all nanofluid samples, i.e., the ratio of the nanofluid thermal conductivity to the basefluid thermal conductivity is also shown in Table 1. For each organization, the data represents the ratio of the mean thermal conductivities of the nanofluid and basefluid. If a participating organization did not measure the basefluid thermal conductivity in their laboratory, a calculation of enhancement was not made. There was reasonable consistency (within ±5%) in the thermal conductivity ratio data among most organizations and for all four sets, including water-based and PAO-based samples.

Comparing the data for samples 3, 4, 5 and 6 in Set 1, it is noted that, everything else being the same, the thermal conductivity enhancement is higher at higher particle concentration, and higher for elongated particles than for near-spherical particles. Comparing the data for samples 1 and 5 in Set 1, it is noted that the thermal conductivity enhancement is somewhat higher for the PAO basefluid than for water. The Set 2 data suggest that the thermal conductivity enhancement is negligible, if the particle concentration is very low, even if metal particles of high thermal conductivity are used. On the other hand, the Set 3 data suggest that a robust enhancement can be achieved, if the particle concentration is high, even if the particle material has a modest thermal conductivity. All these trends are expected, based on the effective medium theory, as will be discussed below.

Table 1 Summary of INPBE results

Sample #		Sample description [a]	Measured thermal conductivity [b] (W/m-K)	Measured thermal conductivity ratio [b] k/k_f
Set 1	Sample 1	Alumina nanorods (80x10 nm), 1% vol. in water	0.627 ± 0.013	1.036 ± 0.004
	Sample 2	De-ionized water	0.609 ± 0.003	n/a [d]
	Sample 3	Alumina nanoparticles (10 nm), 1% vol. in PAO + surfactant	0.162 ± 0.004	1.039 ± 0.003
	Sample 4	Alumina nanoparticles (10 nm), 3% vol. in PAO + surfactant	0.174 ± 0.005	1.121 ± 0.004
	Sample 5	Alumina nanorods (80x10 nm), 1% vol. in PAO + surfactant	0.164 ± 0.005	1.051 ± 0.003
	Sample 6	Alumina nanorods (80x10 nm), 3% vol. in PAO + surfactant	0.182 ± 0.006	1.176 ± 0.005
	Sample 7	PAO + surfactant	0.156 ± 0.005	n/a

Set	Sample			
Set 2	Sample 1	Gold nanoparticles (10 nm), 0.001% vol. in water + stabilizer	0.613 ± 0.005	1.007 ± 0.003
	Sample 2	Water + stabilizer	0.604 ± 0.003	n/a
Set 3	Sample 1	Silica nanoparticles (22 nm), 31% vol. in water + stabilizer	0.729 ± 0.007	1.204 ± 0.010
	Sample 2	De-ionized water	0.604 ± 0.002	n/a
Set 4	Sample 1	Mn-Zn ferrite nanoparticles (7 nm), 0.17% vol. in water + stabilizer	0.459 ± 0.005	1.003 ± 0.008
	Sample 2	Water + stabilizer	0.455 ± 0.005	n/a

Discussion of Results

Equation (1) is valid for well-dispersed non-interacting spherical particles with negligible thermal resistance at the particle/fluid interface. To include the effects of particle geometry and finite interfacial resistance, Nan et al. [47] generalized Maxwell's model to yield the following expression for the thermal conductivity ratio:

$$\frac{k}{k_f} = \frac{3 + \phi[2\beta_{11}(1-L_{11}) + \beta_{33}(1-L_{33})]}{3 - \phi(2\beta_{11}L_{11} + \beta_{33}L_{33})} \qquad \text{Equation 2}$$

where, for particles shaped as prolate ellipsoids with principal axes $a_{11} = a_{22} < a_{33}$:

$$L_{11} = \frac{p^2}{2(p^2-1)} - \frac{p}{2(p^2-1)^{3/2}} \cosh^{-1} p,$$

$$L_{33} = 1 - 2L_{11}, \qquad p = a_{33}/a_{11}, \qquad \beta_{ii} = \frac{k_{ii}^c - k_f}{k_f + L_{ii}(k_{ii}^c - k_f)},$$

$$k_{ii}^c = \frac{k_p}{1 + \gamma L_{ii} k_p / k_f}, \qquad \gamma = (2 + 1/p)R_{bd}k_f/(a_{11}/2)$$

and R_{bd} is the (Kapitza) interfacial thermal resistance. The limiting case of very long aspect ratio in Nan et al.'s theory is bounded by the nanoparticle linear aggregation models proposed by Prasher et al. [36] and Keblinski et al. [48]. Obviously, Equation 2 reduces to Equation 1 for spherical particles (p=1) and negligible interfacial thermal resistance (R_{bd}=0), as it can be easily verified. Equation 2 predicts that, if $k_p > k_f$, the thermal conductivity enhancement increases with increasing particle loading, increasing particle aspect ratio and decreasing basefluid thermal conductivity, as observed for the data in INPBE Set 1. More quantitatively, the theory was applied to the INPBE test nanofluids. Table 2 shows one application for zero interfacial thermal resistance (upper

bound), and one for a typical value of the interfacial resistance, $10\text{-}8$ m^2K/W [49, 50, and 51]. It can be seen that all INPBE data can be predicted by the lower bound theory with <17% error, while the upper bound estimate predicts 90% of the data with <18% error.

The above data analysis demonstrates that our colloidally stable nanofluids exhibit thermal conductivity in good agreement with the predictions of the effective medium theory for well-dispersed nanoparticles. That is, no anomalous thermal conductivity enhancement was observed for the nanofluids tested in this study. As such, resorting to the other theories proposed in the literature (e.g., Brownian motion, liquid layering, aggregation) is not necessary for the interpretation of the INPBE database. It should be noted, however, that the ranges of parameters explored in INPBE, while broad, are not exhaustive. For example, only one nanofluid with metallic nanoparticles was tested, and only at very low concentration. Also, the temperature effect on thermal conductivity was not investigated.

Table 2 Summary of INPBE results versus predictions

Sample #		Sample description [a]	Predicted thermal conductivity ratio [c] k/k_f	
			Lower bound	Upper bound
Set 1	Sample 1	Alumina nanorods (80x10 nm), 1% vol. in water	1.024	1.086
	Sample 2	De-ionized water	n/a	n/a
	Sample 3	Alumina nanoparticles (10 nm), 1% vol. in PAO + surfactant	1.027	1.030
	Sample 4	Alumina nanoparticles (10 nm), 3% vol. in PAO + surfactant	1.083	1.092
	Sample 5	Alumina nanorods (80x10 nm), 1% vol. in PAO + surfactant	1.070	1.116
	Sample 6	Alumina nanorods (80x10 nm), 3% vol. in PAO + surfactant	1.211	1.354
	Sample 7	PAO + surfactant	n/a	n/a
Set 2	Sample 1	Gold nanoparticles (10 nm), 0.001% vol. in water + stabilizer	1.000	1.000
	Sample 2	Water + stabilizer	n/a	n/a
Set 3	Sample 1	Silica nanoparticles (22 nm), 31% vol. in water + stabilizer	1.008	1.312
	Sample 2	De-ionized water	n/a	n/a
Set 4	Sample 1	Mn-Zn ferrite nanoparticles (7 nm), 0.17% vol. in water + stabilizer	1.000	1.004
	Sample 2	Water + stabilizer	n/a	n/a

1.4. Conclusions

An international nanofluid property benchmark exercise, or INPBE, was conducted by 32 organizations participating from around the world. The objective was to compare thermal conductivity data obtained by different experimental approaches for identical samples of various nanofluids. The main findings of the study were as follows:

- The thermal conductivity enhancement afforded by the tested nanofluids increased with increasing particle loading, particle aspect ratio and decreasing basefluid thermal conductivity.
- For all water-based samples tested, the data from most organizations deviated from the sample average by ±5% or less. For all PAO-based samples tested, the data from most organizations deviated from the sample average by ±10% or less.
- The classic effective medium theory for well-dispersed particles accurately reproduced the INPBE experimental data, thus suggesting that no anomalous enhancement of thermal conductivity was observed in the limited set of nanofluids tested in this exercise.
- Some systematic differences in thermal conductivity measurements were seen for different measurement techniques. However, as long as the same measurement technique at the same temperature conditions was used to measure the thermal conductivity of the basefluid, the thermal conductivity enhancement was consistent between measurement techniques.

2. CONVECTION

2.1. Introduction

Several experimental studies on nanofluid single-phase heat transfer have been reported in the literature. Pak and Cho [52] explored alumina-water and titania-water nanofluids in turbulent convective heat transfer in tubes. Xuan and Li [53] investigated turbulent convective heat transfer and flow features of copper oxide in water nanofluids. Xuan and Roetzel [54] considered a heat transfer correlation for nanofluids to capture the effect of energy transport by particle "dispersion". Yang et al. [55] measured laminar convective heat transfer performance of graphite nanofluids in horizontal circular tube. Wen and Ding [56] studied nanofluid laminar flow convective heat transfer and reported significant enhancement in the entry region. Ding et. al [57] observed significant convective heat transfer enhancement of multi-walled carbon nanotube dispersion in water and the enhancement depends on the flow conditions (Reynolds number), carbon nanotube concentration and pH. Heris et. al [58 and 59] studied the effects of alumina and copper oxide nanofluids on laminar heat transfer in a circular tube under constant wall temperature boundary condition. They reported heat transfer coefficient enhancement for both nanofluids with increasing nanoparticle concentrations as well as Peclet number, and observed higher enhancement in alumina nanofluid than copper oxide. He et al. [60] investigated the heat transfer of titania nanofluids in both laminar and turbulent flow, and found the heat transfer enhancement increased with particle concentration and decreasing particle size. Convective heat transfer of alumina nanofluid in microchannels was investigated by Lee et. al [61]. The effective thermal conductivity of 2 volume percent nanofluids was found to increase by only 4-5% and the viscosity by 12% relative to the base fluid. Nanofluid application in microelectronics cooling were recently explored by Chein and Chuang [62] and Nguyen et al [63].

Most of the nanofluid studies reported in the literature have concluded or assumed that nanofluids provide heat transfer enhancement with respect to their respective base fluids. Nonetheless, assessment of what constitutes an enhancement has not been determined on the same basis. An increased heat transfer coefficient may simply reflect the changes in the thermal physical properties of the nanofluid being tested while the models and correlations developed for simple fluids still apply. Unfortunately, none of the above referenced studies uses nanofluids fully characterized in this strict sense. This is the starting point of our paper

The key contribution of this work is in providing experimental data to demonstrate the hypothesis that the nanofluids can be treated as homogeneous mixtures, as such the heat transfer coefficient enhancement is not abnormal, but due to the different mixture properties of the nanofluids. Accordingly our group has measured the convective heat transfer and pressure loss behavior of various nanofluids in laminar and fully-developed turbulent flow [10, and 11].

2.2. Experimental
2.2.1. Apparatus

For the laminar and turbulent studies two unique flow loops were designed and fabricated. References 10 and 11 provide the details of each loop. Figure 2 shows a schematic that is applicable to both the laminar and turbulent convective heat transfer and pressure drop flow loops. The test section was a smooth 316 stainless steel tube that was resistively heated by a DC power supply. T-type thermocouples were spaced axially along the OD of the tube to measure the outer wall temperature. There were also two T-type thermocouples submerged in the flow channel at the inlet and outlet of the heated section to measure the bulk temperature of the fluid. A pump provided the flow that was measured by a turbine flow meter. Heat removal was provided for by heat exchangers connected a chilled water supply. Various valves were included in the system for loading, flow control and discharge of the test fluid. All temperature, flow, and test section resistive heating currents and voltages were acquired by a data acquisition system. The inner wall temperature was calculated assuming radial heat conduction within the tube wall. The heat transfer coefficient was calculated from knowledge of the heat flux and the calculated wall and bulk temperatures at the different axial locations. The viscous pressure loss is measured directly by a differential pressure transducer.
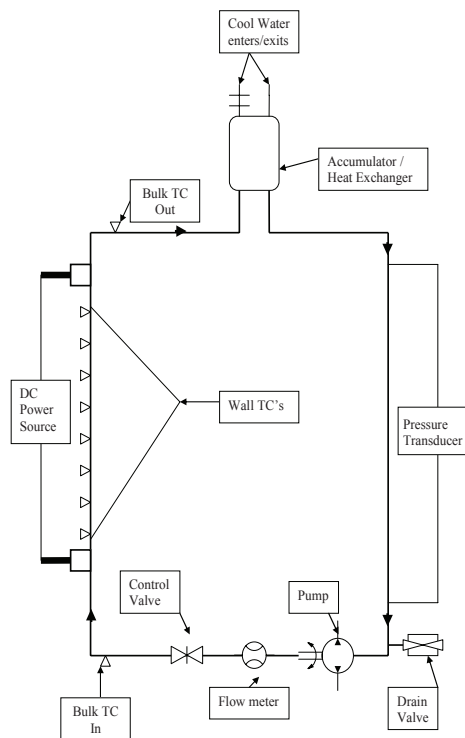
Figure 2 Generic schematic flow loop used in convection work.

2.2.2. *Thermophysical Properties of Nanofluids*

To assess the merits of nanofluids, their thermophysical properties must be known accurately. The density of the nanofluid is by definition:

$$\rho = \phi\rho_p + (1-\phi)\rho_b$$

Assuming thermal equilibrium between the particles and the surrounding fluid, the specific heat is immediately estimated as follows:

$$c = \frac{\phi\rho_p c_p + (1-\phi)\rho_b c_b}{\rho}$$

On the other hand, the thermal conductivity and viscosity of nanofluids have exhibited abnormal behavior and therefore must be measured, as functions of loading and temperature, Full characterization of the fluids colloidal and thermophysical properties was done experimentally, and included measurement of the temperature- and loading-dependent thermal conductivity and viscosity.

The nanofluids used in this work were colloidal alumina AL20SD at 20 percent by weight (wt%) and colloidal zirconia Zr50/15 at 15wt%, purchased from Nyacol® Nano Technologies, Inc. These colloids were used as-received except for dilution using de-ionized water. Characterization was done to assure the specifications of the colloids were as stated by the manufacturer. Inductively coupled plasma spectroscopy (ICP) found there to be only the primary components specified, aluminum and zirconium, in each respective fluid. Only trace amounts of other chemicals were found. Thermogravimetric analysis (TGA) was done to determine the weight loading of the compounds and were found to be as specified by the manufacturer. TGA was also used to determine the exact loading of the diluted samples before and after the flow experiments to assure there was no settling in the loop. The conversion between weight and volume fraction (ϕ) was done through the bulk density of alumina (~3920 kg/m^3) and zirconia (~5500 kg/m^3).

Particle sizing was done using dynamic light scattering (DLS) in combination with transmission electron microscopy (TEM); the methodologies are described elsewhere [64]. It is noted that DLS determines only the equivalent spherical hydrodynamic diameter of the particles. Likewise the TEM can be used only on particles dried out of the colloidal state, and hence could have agglomerations which may not be present in the colloidal state. The DLS results showed that the average particle size for the alumina is about 46 nm and the zirconia is about 60 nm. There is a distribution of size around these averages and the zirconia had small amounts of agglomerations averaging around 200 nm. TEM images confirmed these results are reasonable.

The temperature and loading dependent thermal conductivity was measured with a short transient hot wire apparatus which was validated with various fluids at different temperatures and found to have ±2% accuracy [65]. The transient hot wire apparatus made use of a teflon-coated platinum wire to prevent the occurrence of parasitic currents in the test fluid. The dependence of thermal conductivity on loading was measured for each fluid from zero to the maximum loading, 20 and 15 wt% for alumina and zirconia, respectively. Temperature dependence of the conductivity was measured from 20°C to 80°C, which encompasses the anticipated in-loop conditions. The results are shown in Figure 3 and Figure 4, where the nanofluid thermal conductivity is λ, the thermal conductivity of water is λ_w, and MG refers to the modified Maxwell-Garnett model, applied here to two values of the spheroidal aspect ratio 'c/a', which captures the shapes of our nanoparticles, as per the TEM observations. The measurements show that the loading dependence of thermal conductivity is bracketed by the MG model, while the temperature dependence is the same as that of water. This latter fact is contrary to the findings of Das et al. [18], who reported an abnormally large increase of thermal conductivity in nanofluids and attributed it to Brownian motion of the nanoparticles.

Viscosity was measured by means of a capillary viscometer submerged in a controlled-temperature bath. The viscometer was benchmarked with water at various temperatures and its accuracy was found to be within 0.5%. The alumina and zirconia nanofluid viscosities are shown in Figure 5 and Figure 6, respectively. Note the rapid viscosity increase with particle loading and the independence of the μ/μ_w ratio on temperature. Curve fits were created for the thermal conductivity and viscosity experimental data, to be used in the interpretation of the convective heat transfer data:

Alumina nanofluids
$$\lambda(\phi,T) = \lambda_w(T)(1 + 4.5503\phi)$$

$$\mu(\phi, T) = \mu_w(T) \exp[4.91\phi/(0.2092 - \phi)]$$

Zirconia nanofluids

$$\lambda(\phi, T) = \lambda_w(T)(1 + 2.4505\phi - 29.867\phi^2)$$

$$\mu(\phi, T) = \mu_w(T) \exp[11.19\phi/(0.1960 - \phi)]$$

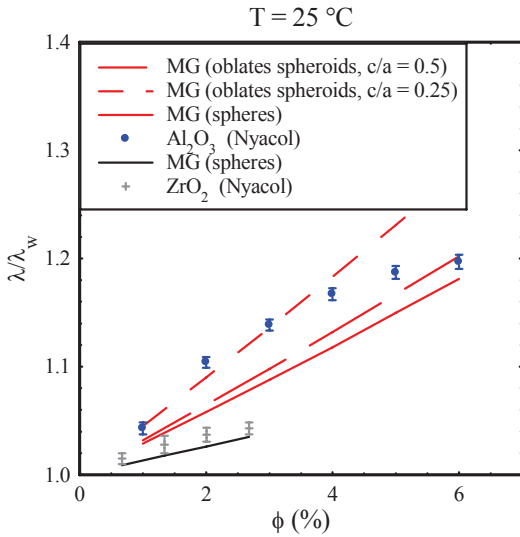These equations apply to our nanofluids and are not of general validity.

T = 25 °C

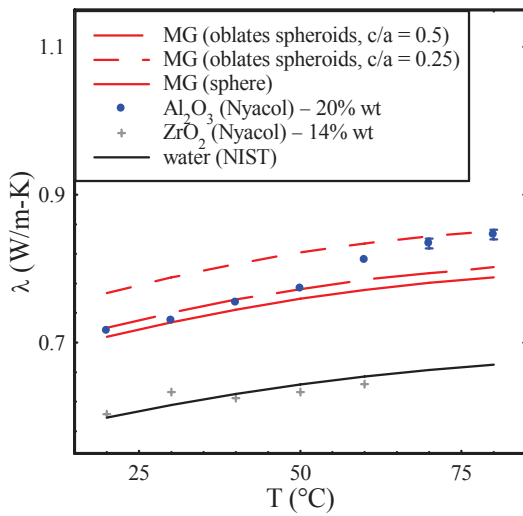

Figure 3 Loading-dependent thermal conductivity.

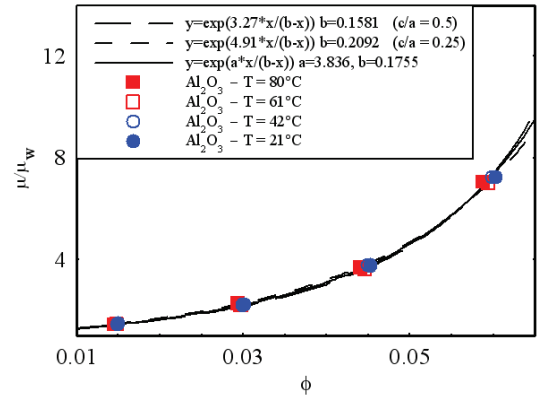**Figure 4** Temperature-dependent thermal conductivity.
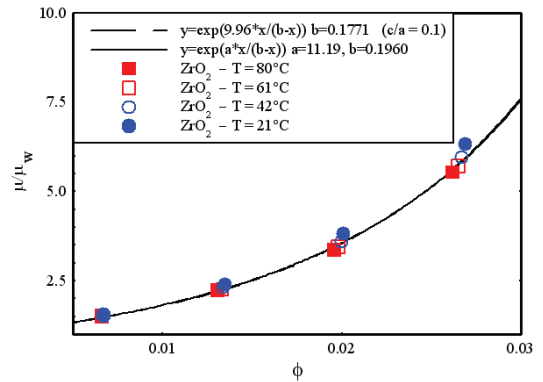

Figure 5. Viscosity of alumina nanofluids.

Figure 6 Viscosity of zirconia nanofluids.

2.3. Results
2.3.1. Heat Transfer
The heat transfer coefficient, *h*, is defined as follows:

$$h = \frac{q''}{T_{wi} - T_b}$$

where q'' is the heat flux on the tube inner wall, T_{wi} is the inner wall temperature, and T_b is the calculated bulk temperature at the axial location of interest. The heat flux is determined from the current and voltage supplied to the test section and its geometry. The inner wall temperature is calculated using the analytical solution of the conduction equation with the measured outer wall temperature and the temperature-dependent thermal resistance of the stainless steel wall. As discussed next, temperature-dependent thermal physical properties of the nanofluids are used in the heat transfer coefficient and dimensionless number calculations based on the local bulk coolant temperature.

2.3.1.1. Laminar
In the laminar study, to allow comparison with theory, we adopted the following curve fits which reproduce the complicated analytical solution for local Nusselt number to within 1% discrepancy [25]:

$$Nu = 1.302\left(\frac{x^+}{2}\right)^{-1/3} - 0.5 \qquad x^+ \le 0.003 \qquad \text{Equation 3}$$

$$Nu = 4.364 + 0.263\left(\frac{x^+}{2}\right)^{-0.506} e^{-41\left(x^+/2\right)} \quad x^+ > 0.003$$

where $Nu = \frac{hD}{k}$

The dimensionless distance is defined as:

$$x^+ = \frac{2\left(x/D\right)}{Re\,Pr} \qquad \text{Equation 4}$$

Re is the Reynolds number $Re = \frac{\rho VD}{\mu}$ and Pr is the Prandtl

number $Pr = \frac{c\mu}{k}$.

Initial tests with deionized water confirmed the heat transfer coefficients were as predicted for laminar flow in a round channel with constant heat flux, as shown in Figure 6. The measurements are normally within 10% of prediction. This result confirms that the loop is working properly. The experimental results for nanofluids are also compared against the theory (Equation 3) based on the dimensionless numbers *Nu* and x^+. This enables the evaluation of nanofluid heat transfer performance on the basis of their respective properties. The temperature- and loading- dependent properties of the fluid as described in experimental section are used to derive these numbers.

Four different alumina nanofluid volumetric loadings (0.6%, 1%, 3% and 6%) were investigated [10]. For brevity the results for 6 v% alumina are shown in Figure 8. The Nusselt numbers are in good agreement with the theory prediction, if the mixture properties are utilized for alumina nanofluid.

The zirconia nanofluid data at three volumetric loadings (0.32%, 0.64%, and 1.32%) were also investigated [10]. The results for the 1.32 v% loading are shown in Figure 9. The data points are again in good agreement with prediction, if the measured mixture properties of the zirconia nanofluid are used.

A significant fraction of the data was acquired over the entrance region of the test section. Detailed analysis of this region [10] further supports that if thermophysical properties of the nanofluid are taken into account existing correlations accurately predict the nanofluids heat transfer characteristics.
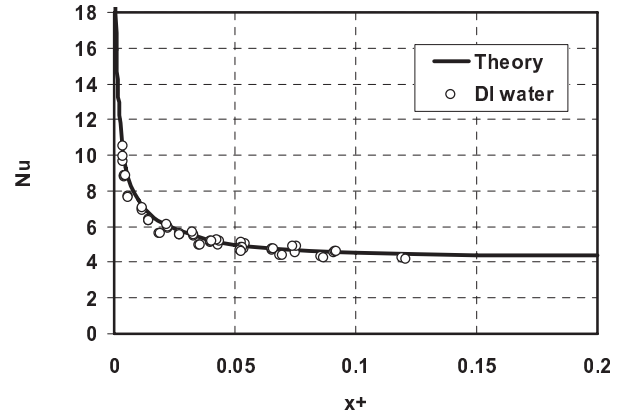
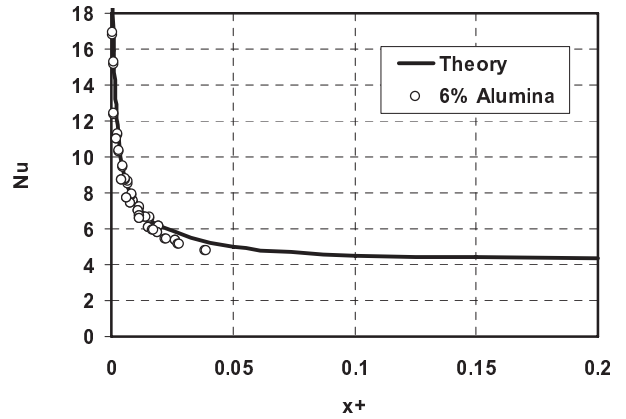**Figure 7** Measured Nusselt numbers versus x^+ for deionized water.

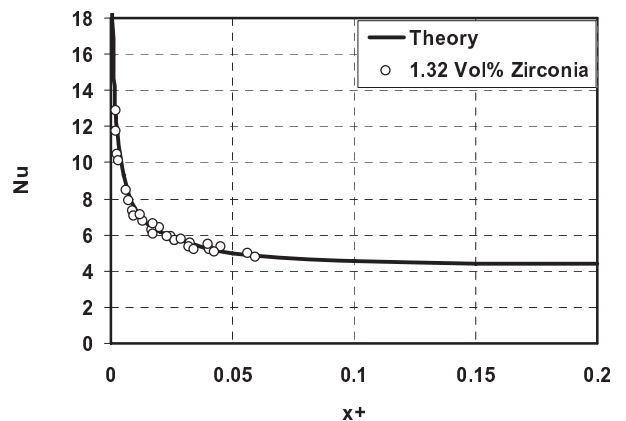**Figure 8** Measured Nusselt numbers versus x^+ for 6 v% alumina nanofluid.

Figure 9 Measured Nusselt numbers versus x^+ for 1.32 v% zirconia nanofluid.

2.3.1.2. Turbulent

The turbulent convective heat transfer behavior of alumina (Al_2O_3) and zirconia (ZrO_2) nanoparticles dispersions in water was investigated experimentally in a flow loop with a horizontal tube test section at various flow rates ($9{,}000 < Re < 63{,}000$), temperatures (21-76°C), heat fluxes (up to ~190 kW/m^2) and particle concentrations (0.9-3.6 and 0.2-0.9 v% for Al_2O_3 and ZrO_2, respectively. The experimental data are compared to predictions made using the traditional single-phase convective heat transfer and viscous pressure loss correlations for fully-developed turbulent flow, Dittus-Boelter and Blasius/MacAdams, respectively.

The convective heat transfer coefficient, h, depends heavily on the fluid properties via the Reynolds, Prandtl and Nusselt number, as per the classic Dittus-Boelter correlation:

$$Nu = 0.023 \, \mathrm{Re}^{0.8} \, \mathrm{Pr}^{0.3}$$

$$h = 0.023 \, \mathrm{Re}^{0.8} \frac{c^{0.3} \lambda^{0.7} \mu^{0.3}}{D} = 0.023 \frac{c^{0.3} \lambda^{0.7} \rho^{0.8} V^{0.8}}{\mu^{0.5} D^{0.2}} \quad \text{Equation 5}$$

As nanofluids typically have higher thermal conductivity and viscosity than their base fluids, Equation 5 suggests that, for a fixed Reynolds number, they will also have a higher heat transfer coefficient. On the other hand, for a fixed velocity, the nanofluid heat transfer coefficient could be either higher or lower than that of the base fluids, depending on the magnitude of the thermal conductivity and viscosity increase. These trends are expected and their explanation does not necessitate invoking any special physical phenomena occurring in nanofluids.

Here we define an *interesting* heat transfer enhancement in nanofluids, as an increase in the measured heat transfer coefficient substantially above that predicted by the traditional single-phase fluid correlation (e.g., Dittus-Boelter). Accordingly, the local heat transfer coefficient was measured for both water, as a base case, and each nanofluid under turbulent fully-developed conditions. The results were compared against the predictions of the Dittus-Boelter correlation, Equation 5, using the temperature- and loading-dependent measured properties of the specific fluid. The benchmark for water at various Reynolds numbers is shown in Figure 10, and can be seen that the experimental data agree well (within ±10%) with the predictions of the correlation.

Alumina nanofluid was measured at three different volumetric loadings (0.9%, 1.8%, and 3.6%) as shown in Figure 11, and zirconia nanofluid at three volumetric loadings (0.2%, 0.5%, and 0.9%) as shown in Figure 12. It can be seen that the Nusselt number is predicted by the Dittus-Boelter correlation to within ±10%, if the nanofluid mixture properties are utilized. No effect of the heat flux on the heat transfer coefficient was observed, as is expected in single-phase forced convection. Water was retested between nanofluid runs in order to assure that there was no significant fouling due to the particles and in fact none was found.
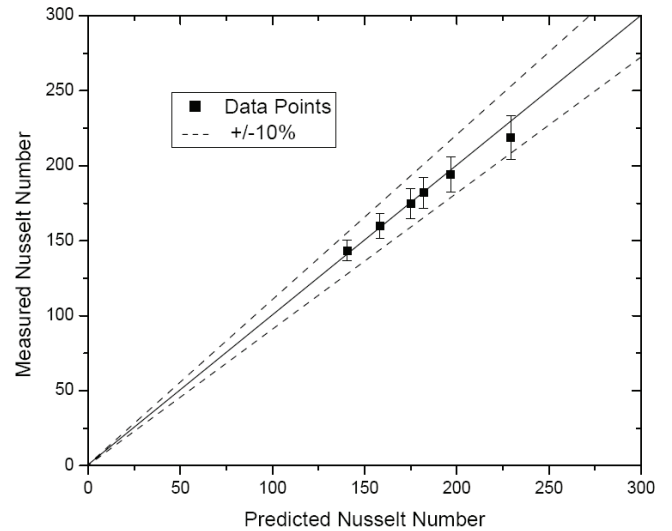

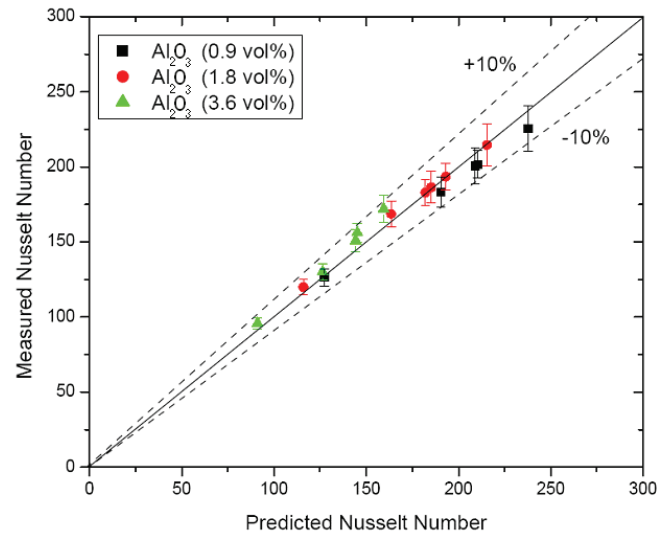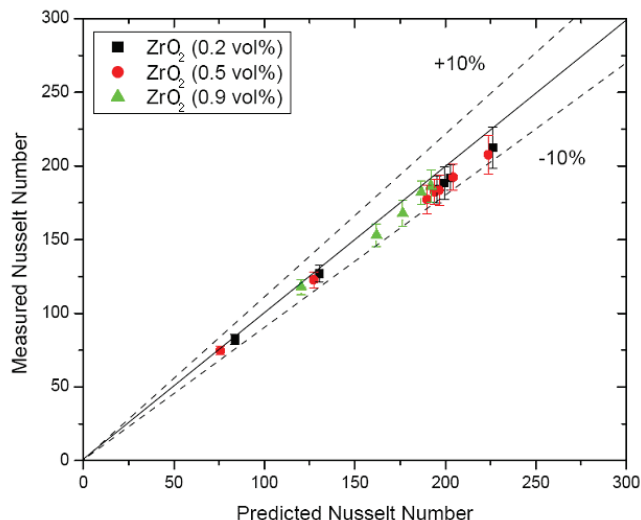**Figure 10** Tube averaged Nusselt number for water tests.

Figure 11 Tube averaged Nusselt number for alumina nanofluid tests.

31

Figure 12 Tube averaged Nusselt number for zirconia nanofluid tests.

2.3.2. *Pressure Drop*

The viscous pressure drop is predicted as

$$\Delta P = f \frac{L}{D} \frac{\rho V^2}{2} \qquad \text{Equation 6}$$

where the friction factor, f, is dependent on the flow conditions, i.e. turbulent or laminar. For both flow conditions the viscous pressure drop was measured for both water, as a benchmark, and each nanofluid. The results were then compared against the theoretical predictions.

2.3.2.1. *Laminar*

For laminar flow in a circular pipe the friction factor, f in Equation 6, is determined from [66]:

$$f = 64/Re \qquad \text{Equation 7}$$

Water results are in good agreement with the prediction of Equation 4. Due to high viscosity, pressure loss of some higher concentration nanofluids exceeded the upper limit of the low-pressure transducer and these test results were not reported here. Figure 13 compares viscous pressure drops of water, alumina and zirconia nanofluid at various concentrations. The measured viscous pressure losses are within ±20% of predictions. By combining Equations (6) and (7), it can be seen that, for a given flow velocity and channel geometry, the pressure loss is proportional to viscosity only. As nanofluids tend to have very high viscosity, viscous pressure losses can become a significant issue when considering nanofluids for practical applications. For example, at 6 v% the viscosity of our alumina nanofluid is about 7.2 times higher than that of water, thus resulting an equivalent magnitude increase in pressure loss.
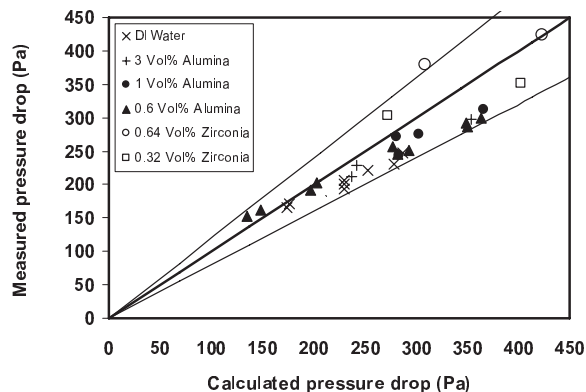
Figure 13 Comparison of measured and predicted pressure losses for water and alumina nanofluid tests.

2.3.2.2. *Turbulent*

For turbulent flow the friction factor, f in Equation 6, is determined from either the Blasius relation

$$f = 0.316 Re^{-0.25}$$

for Re < 30,000 or the McAdams relation

$$f = 0.184 Re^{-0.2}$$

for Re > 30,000 using the temperature- and loading-dependent measured properties of the specific fluid. The benchmark of pressure loss for water at various Reynolds numbers is shown in Figure 14, and can be seen that the experimental data agree well with the theoretical predictions.

Alumina nanofluid was tested at three different volumetric loadings (0.9%, 1.8%, and 3.6%) as shown in Figure 15, and zirconia nanofluid also at three volumetric loadings (0.2%, 0.5%, and 0.9%) as shown in Figure 16. It can be seen that the viscous pressure losses are predicted by the theory to within ±20%, if the nanofluid mixture properties are utilized. A post-test characterization of the nanofluids verified that the particle size and loadings had not changed in the loop.
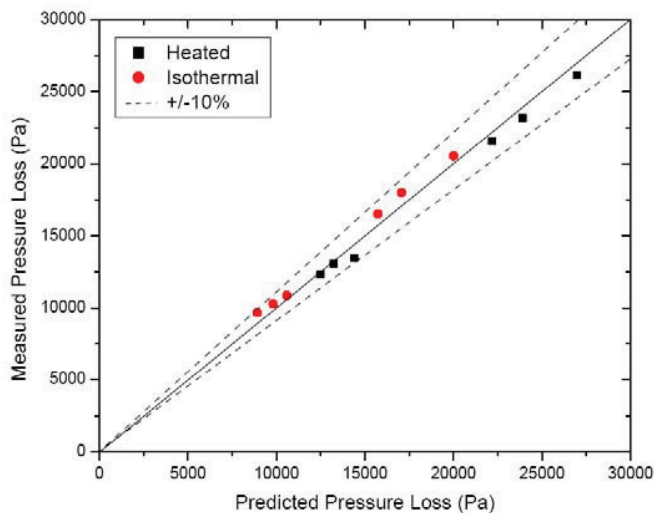
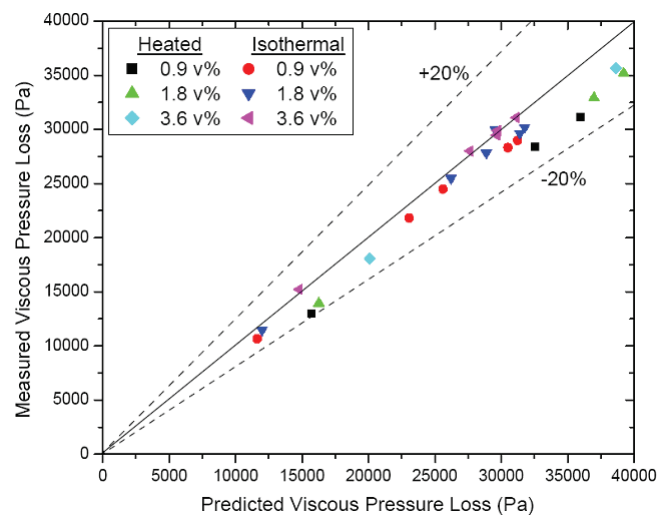**Figure 14** Viscous pressure losses for water tests.

Figure 15 Viscous pressure losses for alumina nanofluid tests.
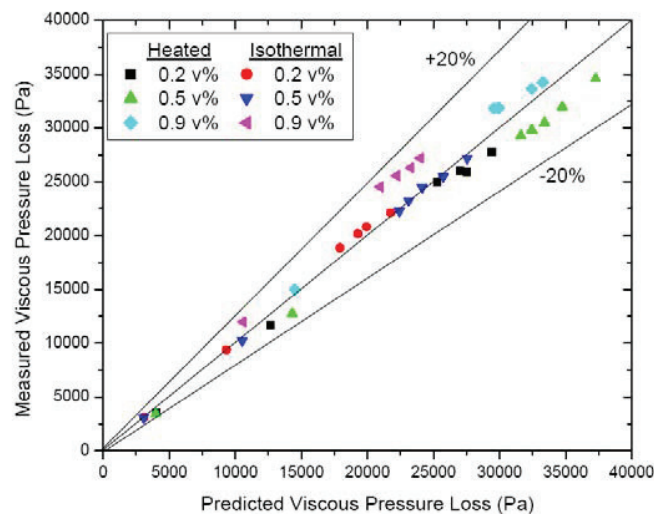

Figure 16 Viscous pressure losses for zirconia nanofluid tests.

2.4. CONCLUSIONS
2.4.1. Laminar

The heat transfer and viscous pressure loss characteristics of alumina-water and zirconia-water nanofluids in laminar flow regime were studied experimentally. It was found that, for given velocity and channel geometry, 6 v% alumina nanofluid heat transfer coefficient can be up to 27% higher than that of water in the entrance region, while the zirconia nanofluid heat transfer coefficient displays a much lower enhancement with respect to water. While heat transfer enhancement of alumina increases with loading, zirconia exhibit a highest enhancement at 3% at 3.5 v% loading. However, when the data are plotted using dimensionless numbers (Nu and x^+), based on the measured properties of the nanofluids, they show good agreement with the predictions of the traditional models/correlations for laminar flow. This suggests that the nanofluids behave as homogeneous mixtures. As such, the heat transfer coefficient enhancement is not abnormal, but simply due to the different mixture properties of the nanofluids with respect to water. Similar conclusions apply to the pressure loss, i.e., the nanofluid pressure loss is higher than water's, but scales linearly with the fluid viscosity, as expected from the traditional pressure loss theory for laminar flow.

2.4.2. Turbulent

The most interesting finding is that the convective heat transfer and pressure loss behavior of the alumina/water and zirconia/water nanofluids tested in fully-developed turbulent flow can be predicted by means of the traditional correlations and models, as long as the effective nanofluid properties are used in calculating the dimensionless numbers. That is, no abnormal heat transfer enhancement was observed. As such, the merits of nanofluids as enhanced coolants depend largely on the trade off between increase in thermal conductivity (determining the desired heat transfer enhancement) and increase in viscosity (determining an undesirable increase in pumping power). A quantitative analysis for our alumina/water and zirconia/water nanofluids has shown that the ratio of heat transfer rate to pumping power for nanofluids is lower than for water [67], because of the dominant effect of the viscosity rise. This is consistent with Pak and Cho's conclusion about their nanofluids [68]. Future research should be directed towards selection of nanoparticle materials, shape and size that would boost the thermal conductivity increase and reduce the viscosity increase. Nanofluids remain suitable for applications in which an increase in pumping power is not of great concern, e.g., thermal management of high-power electronics.

3. BOILING
3.1. Pool Boiling
3.1.1. Introduction

Many important industrial applications rely on nucleate boiling, to remove high heat fluxes from a heated surface. These include cooling of high-power electronics, nuclear reactors, chemical reactors and refrigeration systems, to mention a few. Nucleate boiling is a very effective heat

transfer mechanism, however it is well known that there exists a critical value of the heat flux at which nucleate boiling transitions to film boiling, a very poor heat transfer mechanism. In most practical applications it is imperative to maintain the operating heat flux below such critical value, which is called the Critical Heat Flux (CHF). Obviously, a high value of the CHF is desirable, because, everything else being the same, the allowable power density that can be handled by a cooling system based on nucleate boiling is roughly proportional to the CHF. Therefore, an increase of the CHF can result in more compact and efficient cooling systems for electronic devices, nuclear and chemical reactors, air conditioning, etc., with significant economic benefits in all these applications.

Several studies of CHF and nucleate boiling in nanofluids have been reported in the literature [69, 70, 71, 72, 73, 74, 75, 76, 77, 78, 79, and 80]. The findings can be summarized as follows:

- Significant CHF enhancement (up to 200%) occurs with various nanoparticle materials, including silicon, aluminum and titanium oxides. This is a very significant finding, since such a substantial enhancement in the limit of nucleate boiling is found with little or no change in the thermophysical fluid properties.
- The CHF enhancement occurs at relatively low nanoparticle concentrations, typically less than 1% by volume.
- During nucleate boiling some nanoparticles precipitate on the surface and form a layer whose morphology depends on the nanoparticle materials.
- Some studies report no change of heat transfer in the nucleate boiling regime [69, 71], some report heat transfer deterioration [70, 75] and others heat transfer enhancement [72, 77].

Researchers have carefully reported the experimental data, but they have made few attempts at and little progress in explaining the CHF enhancement mechanism. The main objective is to start developing an insight of the nucleate boiling heat transfer and CHF enhancement mechanisms in nanofluids.

The findings presented in this section are discussed in greater detail in Reference 81. Infrared thermometry was used to obtain first-of-a-kind, time- and space-resolved data [82, 83] for pool boiling phenomena in water-based nanofluids with diamond and silica nanoparticles at low concentration (0.01-0.1 vol%). In addition to macroscopic parameters like the average heat transfer coefficient and critical heat flux (CHF) value, more fundamental parameters such as the bubble departure diameter and frequency, growth and wait times, and nucleation site density were directly measured for a thin, resistively-heated, indium-tin-oxide surface, deposited onto a sapphire substrate. It was found that a porous layer of nanoparticles built up on the heater surface during nucleate boiling which improved surface wettability compared with the water-boiled surfaces. Using the prevalent nucleate boiling and CHF models, it was possible to correlate this improved surface wettability to the experimentally-observed reductions in the bubble departure frequency, nucleation site density, and

ultimately to the deterioration in the nucleate boiling heat transfer and the CHF enhancement.

3.1.2. Methodology
3.1.2.1. Nanofluid Preparation/Characterization
Two nanoparticle materials, i.e. silica (SiO_2) and diamond (C), were selected for these experiments primarily due to their high chemical and colloidal stability. Both nanoparticle types have also previously [84, 85] been shown to have a positive influence on boiling phenomena at the concentrations used in this work. Water-based nanofluids of these nanoparticles were purchased as Ludox TMA from Sigma-Aldrich (silica) and Plasma-Chem Gmbh (diamond). The as-purchased nanofluids were then diluted with deionized water to the low concentrations of interest in these experiments, i.e., 0.1% by volume for silica and 0.01% by volume for diamond. The mean effective diameter of the nanoparticles in the dilute nanofluids was measured with the dynamic light scattering technique and was approximately 34±10nm for the silica nanofluid and 173±10nm for the diamond nanofluid. Various properties relevant to two-phase heat transfer were also measured. The surface tension, thermal conductivity and viscosity of the nanofluids were measured [86, 87] by means of a tensometer, a thermal conductivity probe and a capillary viscometer, respectively. These properties were found to differ negligibly from those of pure water, i.e., within ±4%. At the low concentrations of interest here, the fluid density and heat of vaporization can also be considered unaltered. In summary, the transport and thermodynamic properties of the dilute nanofluids used in these experiments are very similar to those of pure water.

3.1.2.2. Boiling Apparatus
The experiments were conducted at saturation at atmospheric pressure in the facility shown in Figure 17. A 0.7-μm thick film made of Indium-Tin-Oxide (ITO) was resistively heated. Boiling occurred on the upward facing side of this film which had an exposed area of 30x10 mm². The ITO was vacuum deposited onto a 0.4 mm thick sapphire substrate, resistively heated with a DC power supply to control the heat flux at the surface. The cell accommodating the test fluid was sealed, included a condenser, and was surrounded by a constant-temperature water bath to maintain a constant test-fluid temperature by minimizing heat losses to the ambient.

Acquisition of the temperature distribution on the heater surface was accomplished using an infrared (IR) high-speed camera, SC 6000 from FLIR Systems, Inc. The use of an IR camera to investigate boiling heat transfer was pioneered by Theofanous et al [88]. As configured in this study, the IR camera had a spatial resolution of 100 μm, which is more than sufficient to capture the temperature distribution about individual nucleation sites since the typical bubble diameter is on the order of 1000 μm. The capture frame rate was 500 Hz.

While the sapphire substrate is transparent (>85%) to IR light, the ITO has the advantageous property of being opaque in the IR range, as this ensures that all temperature measurements are made on the back (bottom) of the ITO substrate. The thinness of the ITO heater guarantees that the IR camera reading from its bottom was an accurate representation of the

actual temperature on the top (wet side) of the heater surface. Thus, neither the temperature of the fluid, nor the integral temperature through the substrate thickness was measured. This made thermal analysis of the heater, and corresponding temperature measurements straightforward. Use of the IR camera (vs. the more traditional approach based on thermocouples embedded at discrete positions in the heater) enables mapping of the complete two-dimensional time-dependent temperature distribution on the heater surface. Heat loss from the heater bottom via air natural convection was calculated to be negligible (<1%).

During each experiment, the heat flux was increased in discrete steps (25-50 kW/m^2) up to the critical heat flux (CHF). At each intermediate step the temperature map was recorded for 2.0 sec. Since the typical time scale for a bubble nucleation cycle is tens of ms, 2 sec is sufficient to obtain good data statistics. Near the critical heat flux, the heat flux was increased in smaller increments (10-25 kW/m^2), to ensure higher accuracy in capturing the CHF event.

A detailed discussion of the experimental procedure, data reduction procedure and measurement uncertainty is available in a previously published study by the same authors on pool boiling heat transfer in water [82, 83].
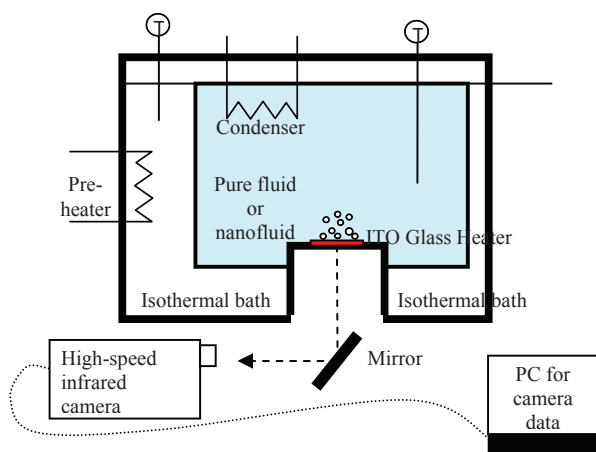
Figure 17 MIT pool boiling facility with infrared thermometry.

3.1.3. Results
Heat Transfer
The nucleate boiling and critical heat flux characteristics of deionized water and water-based nanofluids were studied with infrared thermometry. Pool boiling curves (shown in Figure 18) were generated for the seven (3 pure water and 4 nanofluid) experiments that are discussed in this paper by taking the time average (over 2 sec) and space average (of a 5x5 mm^2 area in the center of the heater) of the IR-measured temperature distribution at a given heat flux. Several generalized conclusions can be immediately inferred by inspecting this figure. First, the effective nucleate boiling heat transfer coefficient for all nanofluids is lower (i.e. deteriorated) compared with the water experiments, since the boiling curves are shifted significantly to the right. This reduction is further

highlighted in Figure 19; here the heat transfer coefficient is calculated from knowledge of the heat flux, the average measured surface temperature, and the bulk fluid temperature (which is the saturation temperature for these experiments)

$$h = \frac{q''}{T_w - T_{sat}}$$

The reduction in nucleate heat transfer coefficient in nanofluids is as much as 50% for a given wall superheat. The second conclusion that can be made is that the value of critical heat flux in nanofluids was significantly higher (~100%) than the average water value. The uncertainty in the CHF values was estimated to be ±10%, which can primarily be attributed to the possibility that CHF could occur between discrete heat flux steps which were always less than 10% of the total heat flux near CHF.

By obtaining time- and space-resolved temperature data during bubble nucleation, the bubble departure diameter and frequency, growth and wait times, and nucleation site density were directly measured. The bubble parameters for each individual nucleation event were tallied. Since boiling is essentially a random phenomenon, for each nucleation site and between nucleation sites, there was a distribution of the parameters; however, we observed that the parameters tend to be distributed normally and narrowly about their mean. Therefore, only the mean values of the parameters for all nucleation sites are shown in Figure 20, Figure 21, Figure 22, Figure 23, and Figure 24. It can be seen that, for a given wall superheat, the nanofluids have significantly lower bubble departure frequency, higher wait time and lower nucleation site density with respect to pure water. The implications of these findings will be discussed here.

Surface Analysis
Scanning Electron Microscope (SEM) analysis of the heater surface revealed that the surface was clean during pure water boiling (Figure 25a), but a porous layer built up during nanofluid boiling (Figure 25b&c). Energy Dispersive Spectrometer (EDS) analysis of the layer confirmed that it was made of the nanoparticle material. The presence of a porous nanoparticle layer due to particle deposition during nucleate boiling is now well known [84, 89]. Confocal Microscopy confirmed that the surface roughness (SRa) and surface index (ratio of actual surface area due to peaks and valleys to the projected area viewed) were higher for nanofluid-boiled surfaces than for pure water-boiled surfaces. The measured surface roughness of the water-boiled heater (SRa=132 nm), was slightly higher than the as-received heater (SRa=30 nm), while it was significantly higher for the nanofluid-boiled surfaces (900-2100 nm). The surface index for water-boiled surfaces was approximately 1.0, and for nanofluid-boiled surfaces ranged from 1.1 to 1.7. These values were smaller than expected given all of the peaks and valleys created by the nanoparticle deposits, but are consistent with other nanofluids results [86, 87].

The porous nanoparticle layer increases the surface wettability, which directly affects boiling phenomena, as will be discussed later. The static contact angle of the as-received heater was approximately 100°, the contact angle of the heaters that were boiled in DI water ranged from 80 to 90°, while the

contact angle of the heaters boiled in nanofluids were significantly lower (6-16°). There is a slight, but statistically significant, trend of the heaters boiled in silica nanofluids having a lower contact angle than those boiled in diamond nanofluids.
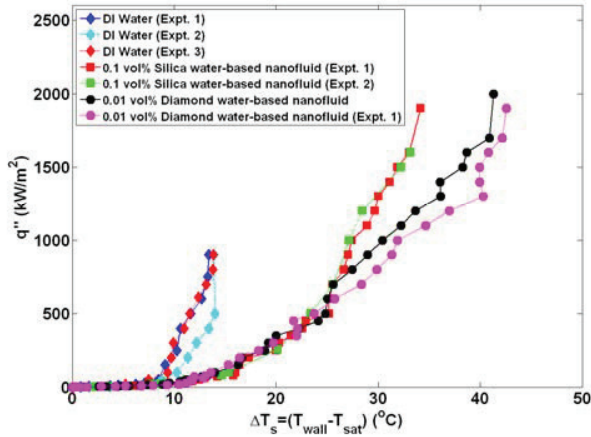

Figure 18 Pool boiling curve for DI water and nanofluids tests. Approximate uncertainty in measurement of q'' and ΔT_s are both 2%. The onset of nucleate boiling (ONB) is at approximately the same superheat (~7°C) for all experiments (i.e. water and nanofluid ONB is very similar).
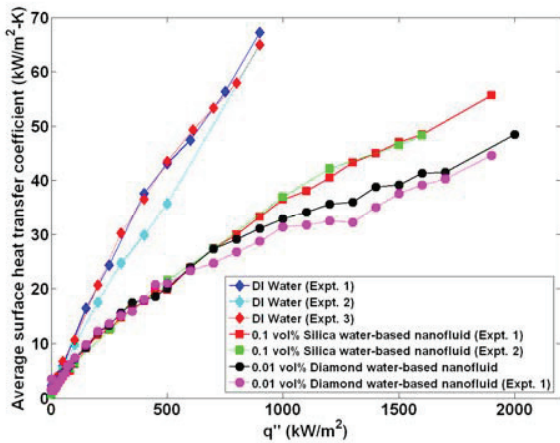
Figure 19 Average wall heat transfer coefficient as a function of applied heat flux (Uncertainty is ±3%).
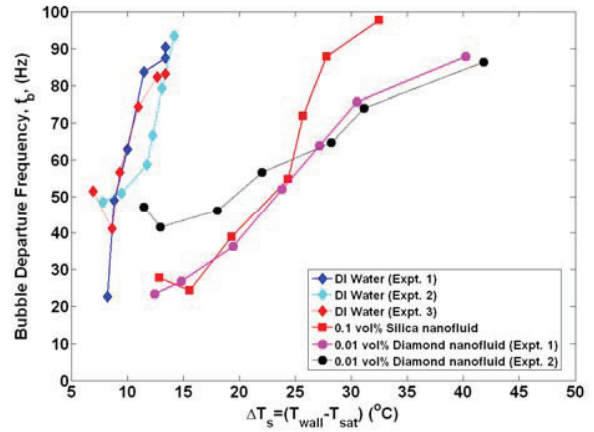
Figure 20 Average bubble departure frequency as measured by infrared thermometry. Uncertainty is ±20%.
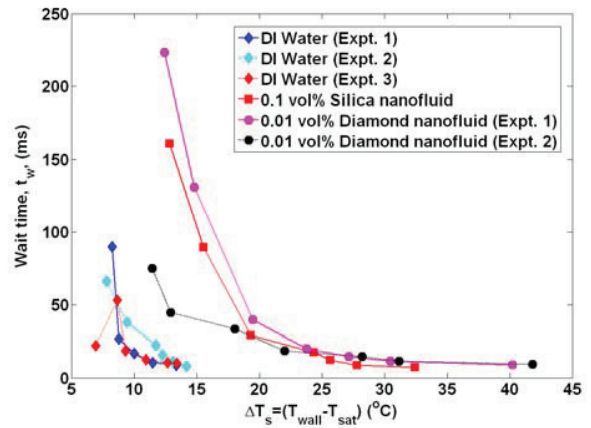
Figure 21 Average wait time as measured by infrared thermometry. Uncertainty is ±20%.
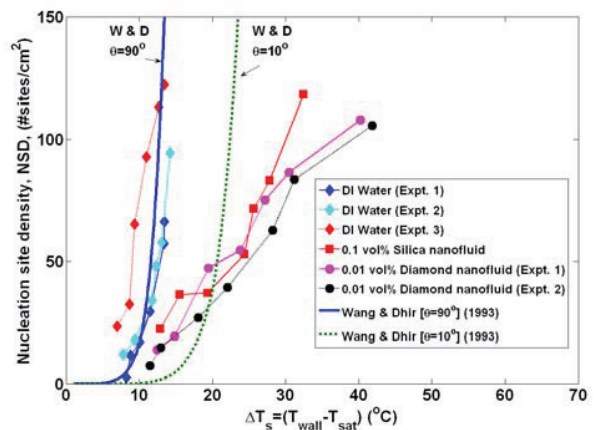
Figure 22 Active nucleation site density as measured by infrared thermometry. Uncertainty is ≤2%.
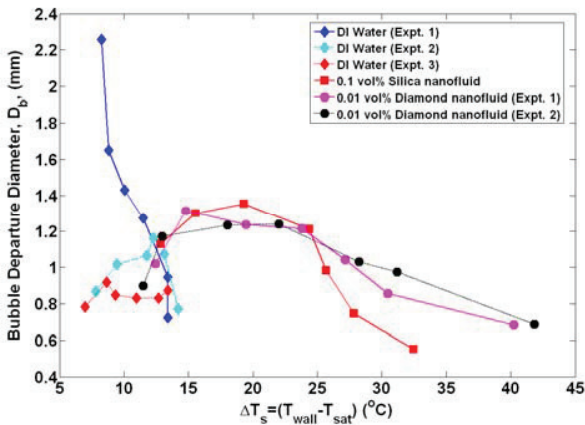
Figure 23 Average bubble departure diameter as measured by infrared thermometry. Uncertainty is ±2%
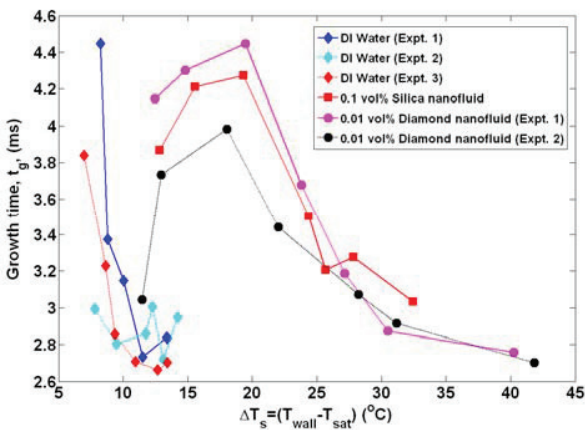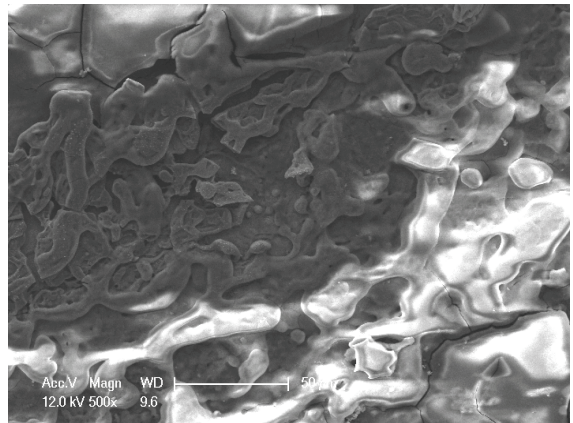

Figure 24 Average growth time as measured by infrared thermometry. Uncertainty is ±20%.
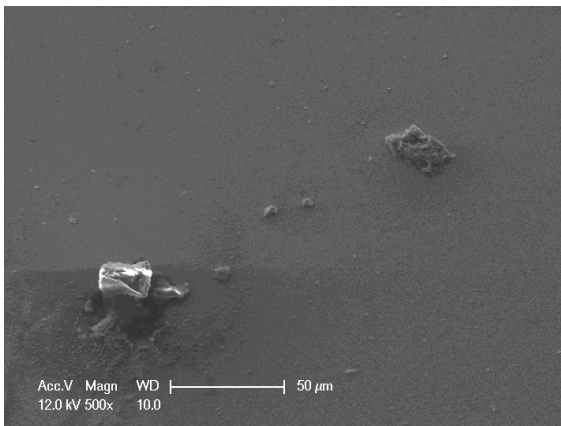

(a)
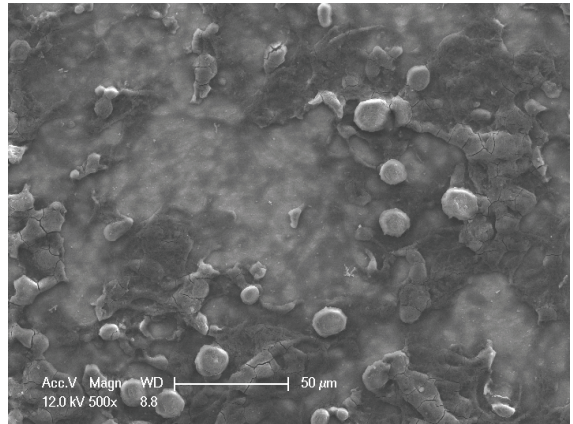
(b)

(c)

Figure 25 SEM images of ITO heater surface after being boiled in DI water (a), 0.01 vol% diamond nanofluids (b), and 0.1 vol% silica nanofluids (c).

3.1.4. Discussion of Results

As presented above, the nucleate boiling heat transfer coefficient and critical heat flux were found to decrease and increase, respectively, in nanofluids. These behaviors are compatible, and related to the surface modification that was observed due to the porous nanoparticle layer deposited via boiling.

3.1.4.1. Nucleate boiling heat transfer coefficient deterioration in nanofluids

Influence of thermal resistance of nanoparticle surface deposit on boiling curves

The infrared camera measures temperatures on the backside of the ITO heating element. The nanoparticles that deposit onto the surface during nanofluid boiling create a thermal resistance, which tends to shift the boiling curve to the right; therefore, it is examined here in some detail. It is possible to estimate the effective thermal conductivity, k_{eff}, of the layer by using Maxwell's [15] effective medium theory as a function of the thermal conductivities of the particle material, k_s, and the pore-filling fluid, k_f, as:

$$\frac{k_{eff}}{k_p} = \frac{1 + 2\beta\varepsilon}{1 - \beta\varepsilon}$$

where

$$\beta = (k_f - k_p)/(k_f + 2k_p)$$

and the porosity, ε, is determined with the particles being the solid phase and the pore filling fluid as the dispersed phase. The interfacial thermal resistance between the nanoparticle material and the pore filling fluid is included in the effective particle thermal conductivity, k_p, as $k_p = k_s + \alpha k_f$, with $\alpha = R_b k_s/d$, and d is the nanoparticle diameter. A conservative value for the interfacial thermal resistance has been suggested by Eapen et al. [90] as $R_b = 2.5 \times 10^{-8}$ Km^2/W. Using a porosity $\varepsilon = 0.74$, and nanoparticle layer thickness of 10 μm (which was shown to be the approximate layer thickness using confocal microscopy), at a heat flux, q"=500 kW/m^2, assuming steam in the pores ($k_s = 0.025$ W/mK), the temperature rise on the ITO IR emitting surface would be 0.01 and 3.1°C for silica and diamond nanoparticle materials, respectively. Since the observed shift in the boiling curve at this heat flux is greater than 15°C, the thermal resistance cannot be the only explanation, even when this analysis has chosen fairly conservative values for porosity. However, a better understanding of the porosity and fluid that fills the pores is required to make a definitive statement on this subject.

Nucleate boiling heat transfer models

The individual bubble parameters jointly determine the macroscopic heat transfer behavior of the surface. To study this behavior, the bubble parameters (D_b, N_{SD}, f_b, t_g, t_w) shown in Figure 20, Figure 21, Figure 22, Figure 23, and Figure 24 were used in the popular heat flux partitioning model (Kurul & Podowski [91]), which has also been labeled as the "RPI Model" after the authors' university.

The model is based on the Bowring [92] scheme of accounting for the various boiling heat transfer mechanisms separately. Both were primarily developed for flow boiling, but have been extended and applied to pool boiling here.

The heat removed by the boiling fluid is assumed to be through the following contributions:

1. the latent heat of evaporation to form the bubbles ($q"_e$)
2. heat expended in re-formation of the thermal boundary layer following bubble departure, or the so-called quenching heat flux ($q"_q$)
3. heat transferred to the liquid phase outside the zone of influence of the bubbles by convection ($q"_c$).

The total partitioned boiling heat flux is obtained through the addition of the three fluxes as:

$$q"_{tot} = q"_e + q"_q + q"_c$$

Each of the partitioned heat fluxes were expressed to account for the contributions of all of the nucleation sites at a given heat flux, as detailed in Gerardi et al. [82]. A comparison of the nanofluids and water total partitioned boiling heat fluxes is presented in Figure 26. These curves represent the predicted boiling curves for each test using *only* the measured bubble

parameters to calculate the heat flux at a given wall superheat. A clear deterioration of the nucleate boiling heat transfer coefficient in nanofluids is seen in agreement with the experimental boiling curve. The dominant heat flux found in the RPI model, the partitioned quench heat flux, $q"_q$, goes as:

$$q"_q \propto f_b N_{SD}$$

A significant reduction in bubble departure frequency and nucleation site density was found in nanofluids boiling (see Figure 20 and Figure 22), which directly correlate to a significant reduction in the heat transfer coefficient predicted by the RPI model. In the next section, the reduction of these bubble parameters is shown to be a result of the surface modification, in particular the increased surface wettability, found for the nanofluid-boiled surfaces.
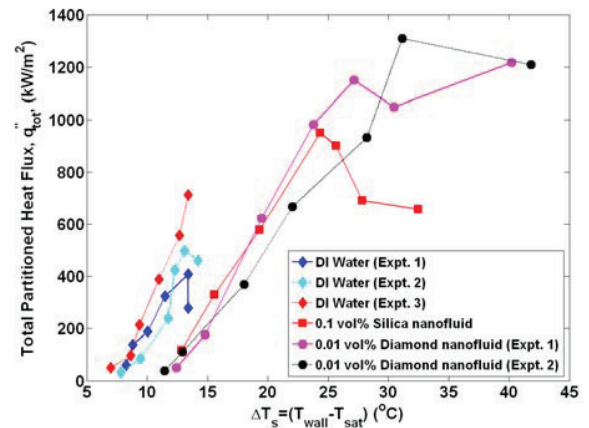
Figure 26 Total partitioned heat flux predicted by the RPI model.

Surface property influences on bubble parameters

The microcavity theory of bubble growth holds that the required superheat (ΔT_{sat}) for bubble nucleation is dependent on the cavity size and the contact angle for fixed fluid properties. It is straightforward to show [83] that for a given set of fluid properties, the relationship between the contact angle and wall superheat goes as

$$\Delta T_{sat} \propto \phi^{1/2}$$

where

$$\phi = \frac{1}{2} + \frac{1}{2}\cos\theta + \frac{1}{4}\cos\theta\sin^2\theta$$

In the limit of a perfectly wetting system, i.e. $\theta = 0°$, the superheat required would be the same as for homogeneous nucleation since $\phi = 1$, while for an extreme non-wetting system, i.e. $\theta = 180°$, no superheat is required for spontaneous bubble growth from a microcavity since $\phi = 0$. This relationship makes it possible to estimate the difference in superheat required for surfaces with two different contact angles assuming all other properties the same.

The sharp reduction in contact angle of nanofluid-boiled surfaces supports the deterioration of the boiling curve, or shift to the right, that was found for nanofluids. The contact angle for nanofluid-boiled surfaces was approximately $\theta \approx 10°$, where

φ≈1, which gives no reduction in the required superheat, while the approximate contact angle of water-boiled heaters was θ≈90° which results in a value of φ=1/2 and a reduction in the required superheat of 1/√2. Thus, the superheat required in water to achieve a given energy of formation is significantly (~1/√2 or 0.707) lower than that for nanofluids. The boiling curve for water is shifted by 27-32°C compared with that of nanofluids at a heat flux of 1000 kW/m², or approximately a factor of 0.44 to 0.52. Thus, the change in contact angle can explain a significant portion of the deterioration of heat transfer coefficient in nanofluids. Note that this analysis is very approximate since the maximum superheats for the highly wetting nanofluid surfaces are under 50°C, while the prediction for homogenous nucleation of water at atmospheric pressure is approximately 220°C.

It was surprising that, for given wall superheat, the nucleation site density for the nanofluids was lower than that of water (Figure 22), given the formation of the nanoparticle-made porous layer on the boiling surface which likely increases the number of available microcavities for nucleation. However, the observed trend can also be explained by the increased wettability of nanofluid-boiled surfaces, as discussed next. Carey [93] reported that the active nucleation site density is related to the minimum interface radius during embryo growth, which in turn, is dependent on the surface contact angle. Wang and Dhir [94] experimentally determined the relationship between contact angle and nucleation site density:

$$N_{SD} \propto N_c (1 - \cos\theta)(\Delta T_{sat})^6$$

where N_c is the number of microcavities per unit surface area, which Wang and Dhir determined empirically. The Wang & Dhir predictions for the nucleation site density for contact angles of θ=10 and 90°, corresponding to water-boiled and nanofluids-boiled surfaces, respectively, are superimposed over the present experimental data in Figure 22. The Wang & Dhir model predicts a significant decrease in nucleation site density with a reduction in contact angle, consistent with the experimental observations. It must be concluded that, in our tests, the effect of wettability reduction more than offsets the increase in the number of microcavities, which presumably is brought about by the porous layer.

Additionally, if a greater superheat is required for bubble nucleation in nanofluids, then the wait time (or time it takes for transient conduction to heat the superheated boundary layer to the required superheat), would be expected to be higher than that of water, as was observed. Since the wait time comprises a significant portion (50-98%) of the ebullition cycle, it follows that the bubble departure frequency of nanofluids would be lower ($f_b=1/(t_w+t_g)$) than water at a given superheat, as was observed. The additional time it takes to heat the boundary layer of nanofluids to the required superheat can be estimated using a semi-infinite solid analysis assuming a constant heat flux. The boundary layer is idealized to re-form instantly on the heater surface and be heated through one-dimensional conduction with no additional convective effects. The thickness of the thermal boundary layer is assumed to equal to 200 μm for both water and nanofluids, based on analysis in Gerardi [83]. From Figure 18, for a wall superheat of 14°C, the wall heat flux was approximately 900 and 100

kW/m² for water and nanofluids, respectively. The time it takes for the entire boundary layer to reach the corresponding superheat is found to be 61 and 280 ms for water and nanofluids, respectively. While these absolute values do not match the experimental data shown in Figure 21, an order of magnitude increase in wait time for nanofluids at a given superheat was observed.

Thus, the increased surface wettability found for the nanofluid-boiled surfaces seems to be the root cause of the deteriorated nucleate boiling heat transfer coefficient in our experiments.

3.1.4.2. Critical heat flux increase in nanofluids

Effect of wettability on CHF

The hydrodynamic instability theory developed by Kutateladze-Zuber [95] suggests that CHF is dependent only on fluid properties. Since nanofluids at the low concentrations used in this study have fluid properties nearly identical to pure water, the hydrodynamic instability theory would predict that nanofluids and water have the same value for CHF, which is contrary to the experimental evidence. It is interesting to note that recently, the reliability of the hydrodynamic instability theory has been questioned even for pure fluids (e.g. Theofanous et al. [96]) based on experimental evidence that micro-hydrodynamics at the heater surface represent the key physics of the burnout process. Three other theories take into account surface wettability on CHF: the macrolayer dryout theory (Haramura & Katto [97]; Sadasivan et al. [98]), hot/dry spot theory (Kandlikar [99]; Theofanous & Dinh [100]; Kim et al. [12]), and the bubble interaction theory (Rohsenhow and Griffith [101]; Kolev 102, 103]). A thorough review of these theories is presented by Kim et al. [12], where they showed how the hot/dry spot theory of Kandlikar [99] supports an increase in CHF due to the increased surface wettability of nanofluid-boiled surfaces. Gerardi [83] used the macrolayer dryout theory of Sadasivan et al. [98], and the bubble interaction theory of Kolev [103] to additionally link increased surface wettability with CHF increase.

A discussion of the hot/dry spot theory CHF theory of Kandlikar incorporating measured bubble parameter data to support the influence of the contact angle on CHF was chosen here to convey how the measured bubble parameter data can be used to probe the physical mechanisms in nucleate boiling.

Kandlikar [99] considered the force balance on the left half of a single bubble at the moment where the force due to change in momentum from evaporation (or evaporation recoil force), F_M, is higher than the sum of the hydrostatic pressure (F_G) and surface tension forces ($F_{S,1}$ & $F_{S,2}$) holding the bubble in its spherical shape (see Figure 27). This causes the liquid-vapor interface to move rapidly outward along the heater surface, resulting in CHF. Kandlikar assumes that CHF occurs when the force due to the momentum change, F_M, pulling the bubble interface away from the bubble center exceeds the sum of the forces holding the bubble intact, $F_{S,1}$, $F_{S,2}$ and F_G. The force balance at this moment is:

$$F_M = F_{S,1} + F_{S,2} + F_G$$

The present analysis obtained discrete data for the bubble diameter at all wall superheats. The surface contact

angle is also known, thus it is possible to calculate these bubble forces at a given superheat without relying on empirical models or correlations. The average bubble diameter at a given superheat is used for this analysis. The ratio of the force due to the momentum change over the sum of the gravity and surface tension forces is plotted for all superheats in Figure 28.

While none of the experiments reach a value of unity, which is the condition predicted by Kandlikar for CHF, it is remarkable how all cases show the same trend. The value of the force ratio is between 0.33-0.50 at CHF for all cases. The fact that a value of unity is never reached is not entirely surprising since there are a number of assumptions in Kandlikar's model, including the bubble shape, area of bubble influence and the average diameter. However, there is a very clear shift to the right for the nanofluid data, illustrating the reduction in the momentum force with decreasing contact angle. This analysis clearly demonstrates the effect of contact angle on the forces theorized to dominate at CHF. It also is the first time actual experimental data on bubble parameters has been used to quantify these forces and relate them to the CHF condition.

Kandlikar uses the force balance at CHF to solve for the heat flux where CHF is reached, q''_{CHF}:

$$q''_{CHF} = K\rho_v h_{fg} \left[\frac{\sigma g(\rho_l - \rho_v)}{\rho_v^2} \right]^{1/4}$$

where

$$K = \left(\frac{1+\cos\theta}{16} \right) \left[\frac{2}{\pi} + \frac{\pi}{4}(1+\cos\theta)\cos\varphi \right]^{1/2}$$

A comparison of Kandlikar's predicted CHF values with the experimental data is shown in Figure 29, with good qualitative agreement between the two. Thus, we have experimentally confirmed that the hot/dry spot theory of Kandlikar supports an increase in CHF due to an increase in surface wettability through direct measurement of bubble parameters. The CHF result is consistent with that reported in Truong et al. [86] for alumina, zinc-oxide, and diamond nanofluids.
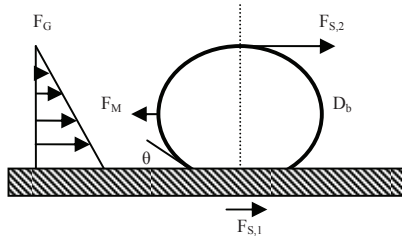
Figure 27 Forces due to surface tension, gravity, and momentum acting on a bubble parallel to the surface (adapted from Kandlikar, 2001).
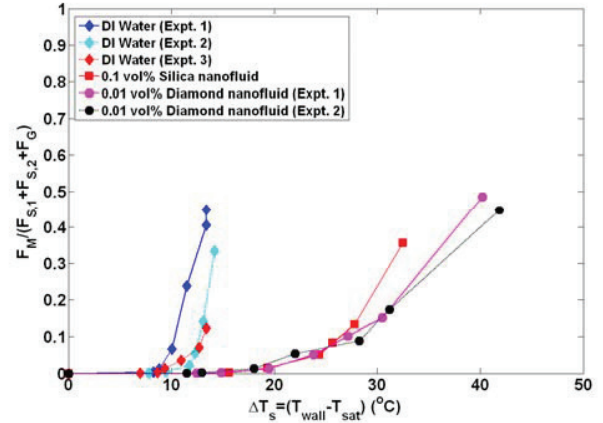
Figure 28 Ratio of F_M and $(F_{S,1} + F_{S,2} + F_G)$ vs. wall superheat. The average bubble diameter, Db, at a given superheat is used as input along with the contact angle and heat flux.
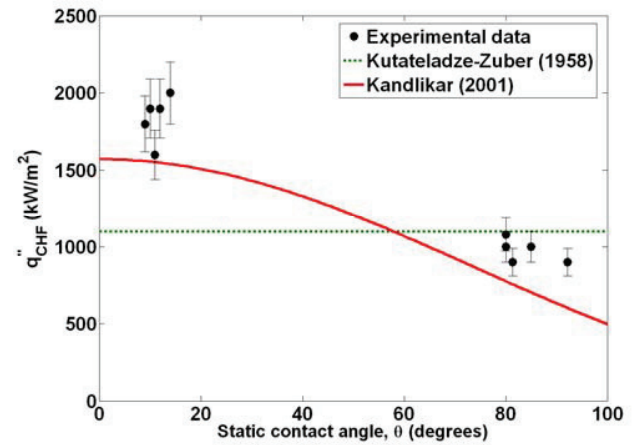
Figure 29 Effect of contact angle on critical heat flux.

Effect of other surface changes on CHF

In addition to increasing the surface wettability, the nanoparticle layer deposited on the surface alters the thermal properties of the surface. The particle layer may promote radial heat dissipation of a local hot spot via conduction, alter liquid replenishment to the surface through capillary wicking through the thin porous layer, or increase surface-to-fluid heat transfer through fin action. Each of these possibilities was considered by Gerardi [83] for the surfaces and conditions used in these experiments. The radial heat dissipation and fin-effect were ruled out as major contributors to CHF enhancement. The porous effect was not studied in detail since porosity was not directly measured in this study. However, Kim and Kim [89] explored the effect of porous nanoparticle layers on CHF due to capillary wicking, and showed that a portion of the CHF increase could be explained by capillary wicking.

3.1.5. Conclusions

Infrared thermometry was used to obtain time- and space-resolved information on nanofluid pool boiling

phenomena. This approach provides a detailed method for investigating the fundamentals of nucleate boiling. Data on bubble departure diameter and frequency, growth and wait times, and nucleation site density were measured for all nucleation sites on the heater surface. The experimentally determined decrease in nucleate boiling heat transfer and increase in critical heat flux were examined in detail with this method. The main findings of the study are as follows:

- The nanoparticle layer increases the heater surface wettability which was shown to be responsible for the observed increase in wait time between bubble nucleation events (thus lower departure frequency) and lower nucleation site density.
- The RPI heat flux partitioning model, directly informed by our bubble parameter experimental data, suggests that the decrease in bubble departure frequency and nucleation site density are responsible for the observed deterioration in the nucleate boiling heat transfer coefficient for nanofluids.
- Kandlikar's hot/dry spot theory for CHF, to which our data on nucleation site density, bubble departure diameter and frequency were directly fed, suggests that the reduction in contact angle sharply reduces the momentum force acting on a bubble, for a given wall superheat, which delays CHF.

3.2. Quenching
3.2.1. Introduction

Quenching refers to the rapid cooling of a very hot solid object by exposure to a much cooler liquid. The heat transfer rate during the quenching process is limited by the occurrence of film boiling, in which a stable vapor film blankets the surface of the hot object, thus creating a very high resistance to energy transfer. An acceleration of the transition from film boiling to nucleate boiling is often desirable, as it results in a much higher heat transfer rate. Dispersing nanoparticles in water could be a means to accelerate that transition and, more generally, enhance heat transfer during the quenching process, as explained next. Reference [14] provides much greater detail of the quenching study discussed in this section.

3.2.2. Experimental
3.2.2.1. Nanofluids Preparation

Three nanoparticle materials were investigated in this study, i.e., alumina (Al_2O_3), silica (SiO_2), and diamond (C). Water-based nanofluids of these three materials were purchased from Nyacol (alumina), Sigma-Aldrich (silica), and PlasmaChem (diamond). The as-purchased nanofluids were then diluted with deionized water to the low concentrations of interest for the quenching experiments, i.e., 0.001%, 0.01% and 0.1% by volume. For practical applications a low particle concentration is very desirable, as the properties of the dilute nanofluids (particularly viscosity) stay similar to those of water, and the nanofluids typically remain transparent.

3.2.2.2. Apparatus

Figure 30 shows a schematic of the experimental setup for the quench tests. It consists of the test sample (sphere), the furnace, the air slide, the quench pool, and the data acquisition system. A radiant furnace with a maximum temperature of 1500°C is used to heat the test sample. A DC power supply (25V, 150A) is used to power the furnace. A B-type sheathed thermocouple is mounted inside the furnace to monitor the temperature. A pneumatic air slide moves the test sample between the furnace and the pool with the stroke length of 200 mm. Pressurized air near 600 kPa is used to operate the slide. The average downward velocity of the sample is about 0.5 m/sec, which is measured with a high-speed camera. The time to move the heated sample from the furnace to the pool is about 0.4 sec. The quench pool is 95 mm × 95 mm rectangular vessel having depth of 150 mm, which has an effectively infinite thermal capacity with respect to the test sample. It is made of Pyrex glass for visual observation of the quenching phenomena. The pool is placed on a hot plate with a maximum power of 800 W. The temperature of the quench pool is maintained with a feedback control of the hot plate and a Pt-100 ohm RTD sensor immersed in the pool. An Agilent 34980A data acquisition system and a PC are used for gathering and storing temperature data from the thermocouple within the test sample. Visualization of the quenching process phenomena is carried out by a high speed CMOS camera (Vision Research Phantom V7.1).
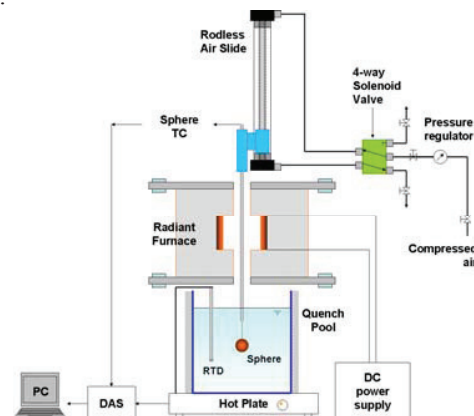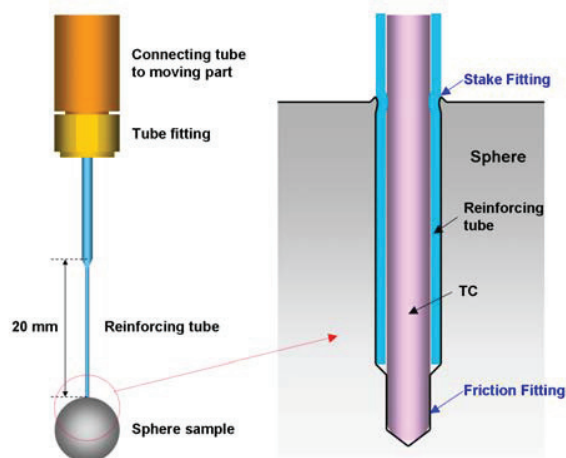

Figure 30 Schematic of the experimental apparatus.

Figure 31 Schematic of the test sample assembly.

3.2.2.3. Test Samples

Figure 31 shows the details of the test samples for the quenching experiment. The test sample consists of a metal sphere, a thermocouple to record the temperature at the center of the sphere, and a reinforcing precision tube to mechanically support them. The sphere materials selected for this study are stainless steel (SS) and zircaloy (Zry), a zirconium-based alloy used as cladding material in the fuel rods of nuclear reactors. Their as-received surface roughness is 0.6 μm and 3.1 μm, respectively. Each sphere is drilled to the center creating a hole stepped from 0.9 mm to 0.5 mm in diameter. A 0.5 mm-diameter K-type sheathed ungrounded thermocouple with the measurement uncertainty of ±1°C is inserted to the bottom of the hole by friction fitting. This technique ensures a good thermal contact with the sphere, and thus minimizes the thermocouple response time, so the rapidly-varying temperature of the sphere can be acquired correctly. A reinforcing tube of 0.6 mm ID and 0.89 mm OD is inserted between the 0.5 mm-diameter thermocouple and the 0.9 mm-diameter hole to mechanically support the test sample. A staking technique – hitting the edge with a sharp tool – is used to connect the tube and the sphere (See Figure 31). The reinforcing tube is connected to the main connecting tube via a tube fitting.

The reinforcing tube is a path of conduction heat loss during the experiments, which should be minimized. The ratio of the reinforcing tube diameter to that of the sphere is very low (0.09), so conduction losses are negligible. The length of the tube is also an important design parameter because vigorous boiling on the sphere surface causes the sphere to vibrate, which may affect boiling itself. Based on an analysis of mechanical vibration of the rod-sphere system, the length of the precision tube was selected to be 20 mm.

3.2.2.4. Procedure

A fresh sphere is thoroughly rinsed with acetone, ethanol, and distilled water before every quenching test. The test sphere is heated up to the initial temperature (~1030°C) in the radiant furnace, and then is plunged into the quench pool with an immersion depth of 6 cm, where the boiling phenomena occurring on the sphere should not be influenced by wavy motion of the free liquid surface due to vigorous vapor flow. The temperature-time history of the sphere is acquired during the cool down. When the sphere has reached thermal equilibrium with the quench pool, the test is over. The same sphere can be reheated and re-quenched, to investigate the effect of surface changes that may have occurred during the previous quench test. This process has been repeated up to seven times, as will be explained in the next section. Pure water and nanofluids are used as the cooling liquid at saturated and highly subcooled (ΔT_{sub}=70°C), always at atmospheric pressure.

3.2.3. Saturated Results

Figure 32 shows a typical temperature-time history (quenching curve) of a SS sphere quenched in saturated water without nanoparticles. The temperature of the quenched sphere

decreases experiencing various heat transfer modes, i.e., film boiling, transition boiling, nucleate boiling, and natural convection. The general shape of the quenching curve can be predicted qualitatively from a simple energy balance for the sphere:

$$\rho c V \frac{d\Delta T}{dt} = -q'' S \qquad \text{Equation 8}$$

where ρ and c are the sphere density and specific heat, respectively, V and S are the sphere volume and surface area, respectively, ΔT is the temperature difference between the sphere and the pool, and $q''(\Delta T)$ is the heat flux at the surface of the sphere at ΔT. Differentiating Equation 8 with respect to time, one gets:

$$\frac{d^2\Delta T}{dt^2} = \frac{S}{\rho c V} \frac{dq''}{d\Delta T} \cdot \left(-\frac{d\Delta T}{dt} \right)$$

Since the sphere is cooling down, the factor $\left(-\frac{d\Delta T}{dt} \right)$ is always positive, thus the curvature of the quenching curve depends only on the slope of the heat flux curve with respect to temperature. Note that $q''(\Delta T)$ is the boiling curve, therefore we have the following:

- The initial section of the quenching curve corresponds to film boiling and thus has a positive curvature
- The Minimum Heat Flux (MHF) point, or Leidenfrost point, is where the quenching curve has its first inflection point
- Transition boiling corresponds to the section of the curve with negative curvature
- The CHF point corresponds to the second inflection point
- The final section of the quenching curve represents nucleate boiling and natural convection, and has a positive curvature.

The various heat transfer regimes were recorded with the video camera, and the results are shown in Figure 32. In film boiling the sphere is completely blanketed with the stable vapor film, as seen in frame (a). As the sphere temperature decreases, the vapor film becomes thinner but remains stable (frame (b)). The MHF point is shown in frame (c), and marks the start of transition boiling, which is shown in frames (c) and (d). Note that some areas of the sphere surface are in contact with the liquid while some are still covered with the vapor film. This behavior is typical of transition boiling. The CHF point is shown in frame (e), and marks the start of the nucleate boiling regime. Note the vigorous boiling action here. Finally, as the sphere temperature asymptotically converges to the temperature of the surrounding liquid, the number of bubbles produced at the surface decreases, as seen in frame (f), until the bubbles disappear completely, which signals the occurrence of single-phase convective heat transfer.

Prior to the nanofluid tests, repeated quench tests were performed in pure water, to establish the base cases. Figure 33 shows the results of these initial tests with both a SS sphere and a Zry sphere. It can be seen that the quenching curve is reasonably repeatable with some minor data scattering in the transition and nucleate boiling regions, likely due to the effect of surface oxidation under repeated heating and quenching cycles from >1000°C to room temperature. The brief plateau at

high temperature in the quenching curves of the Zry spheres is due to a specific heat spike corresponding to the transition from the beta to alpha phase of zirconium, which occurs at around 860°C. Also, it can be noted that the quenching test duration for Zry spheres is roughly half that of SS spheres, which is due to the different thermal capacity (ρc) of the materials, i.e., ~2×10^6 J/m^3-K for Zry vs ~4×10^6 J/m^3-K for SS.

  Figure 34 shows the SS sphere quenching curves for alumina nanofluids at different concentrations (0.001, 0.01, and 0.1% by volume) and, at each concentration, for subsequent repetitions. All the curves for the lowest concentration nanofluid fall within the data scattering of the pure water reference case. At the higher concentrations the curves from the first run also overlap with the water data. This suggests that the nanoparticles present in the fluid have little or no effect on the quenching behavior of a fresh sphere. However, the curves from the subsequent repetitions exhibit a dramatic shift to the left. That is, the end of film boiling occurs significantly earlier in the process and at a significantly higher temperature. The shift is strongest at the highest nanoparticle concentration (0.1 vol%) and grows with each repetition. Finally the quenching duration in the seventh test at 0.1 vol% is shortened to about 50% of the typical time required to cool the hot sphere in pure water. High speed visualization of the seventh run at 0.1 vol% (see Figure 34d) reveals an interesting fact: nucleation of vapor bubbles intermittently occurs at high temperatures, with readings from the thermocouple in the center of the sphere as high as 450°C, which are typically associated with the stable film boiling region. Such intermittent nucleation of bubbles disrupts the vapor film around the sphere and promotes early cooling of the hot sphere, which is consistent with the quenching curve data.

  Figure 35 shows the quenching curves of SS and Zry spheres for alumina, silica and diamond nanofluids (all at 0.1 vol% concentration). While the results obtained with the two different sphere materials show qualitatively identical trends for the same nanoparticle material, the quenching acceleration strongly depends on the nanoparticle material used. Specifically, the diamond nanofluid does not accelerate the quenching process nearly as much as alumina and silica nanofluids do.
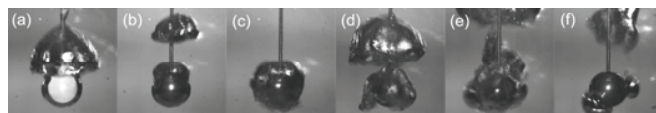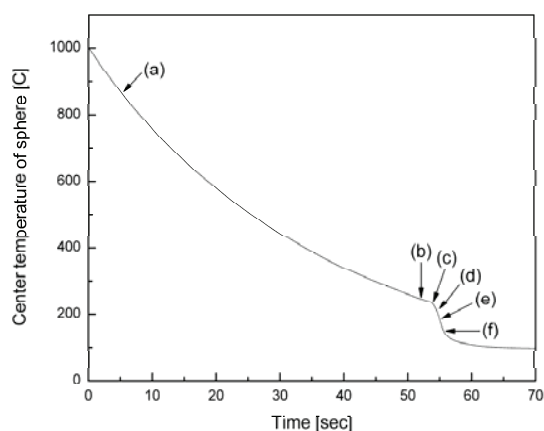

Figure 32 Typical temperature-time history and quenching boiling phenomena on a SS sphere in pure water at saturated condition.
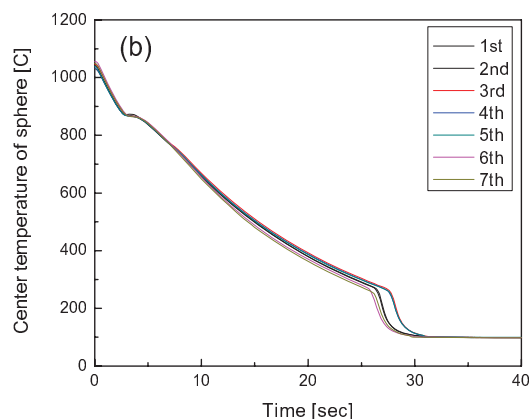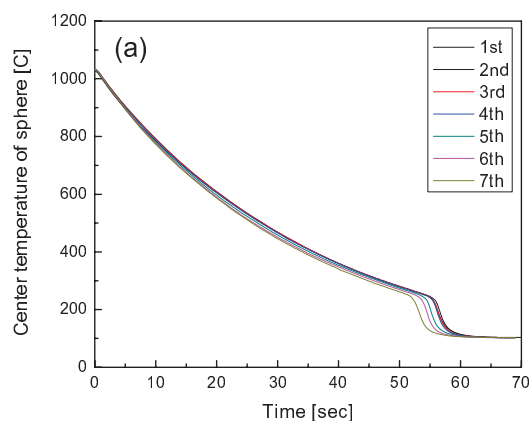

Figure 33 Cooling curves for repetitive runs of (a) SS sphere and (b) Zry sphere in pure water at saturated condition.
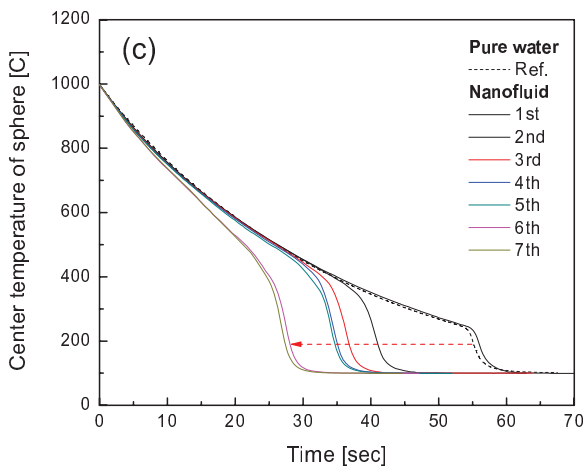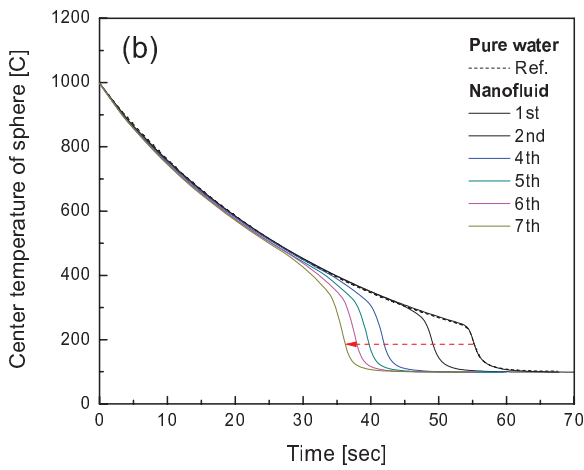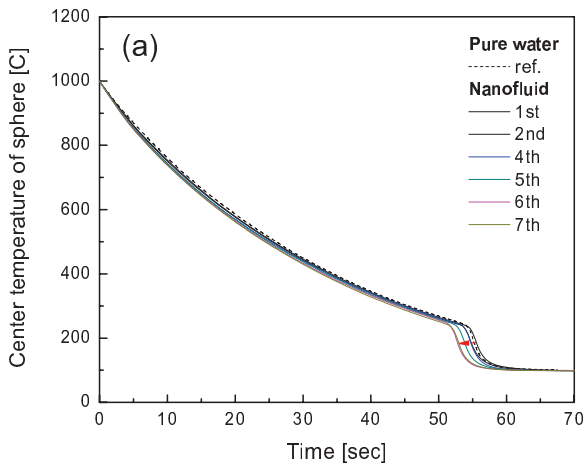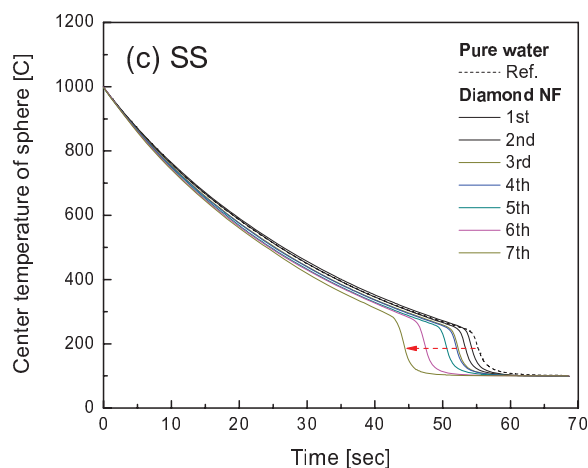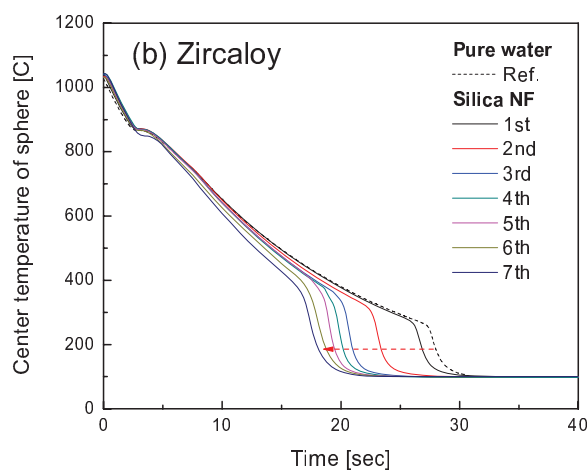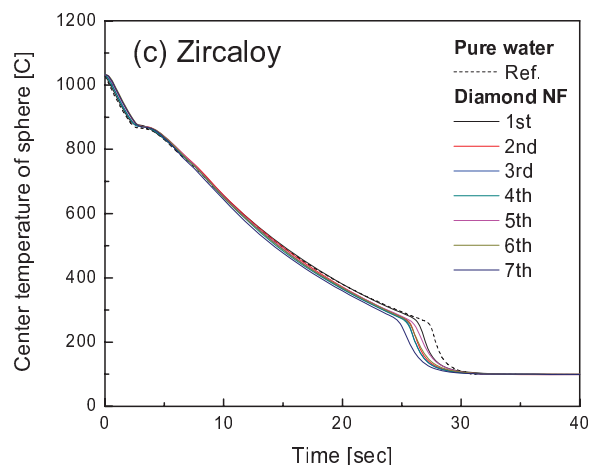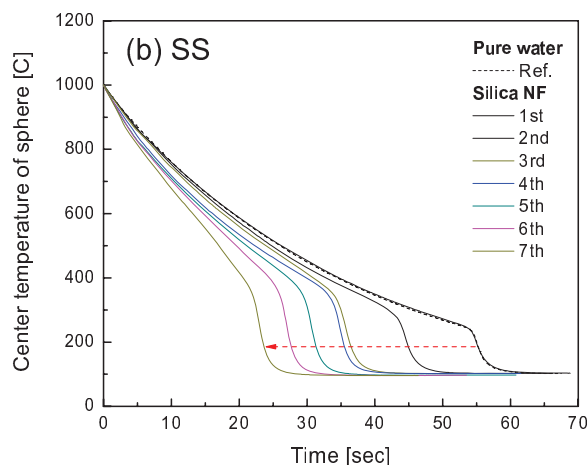
Figure 34 Quenching curves for SS sphere repetitive runs in alumina nanofluids of (a) 0.001, (b) 0.01, and (c) 0.1 vol% concentration at saturated condition, and (d) photographs of intermittent bubble nucleation in the film boiling region near 22 sec after the start of the 7th run for the 0.1 vol% nanofluid. The time interval between frames is 20 ms.
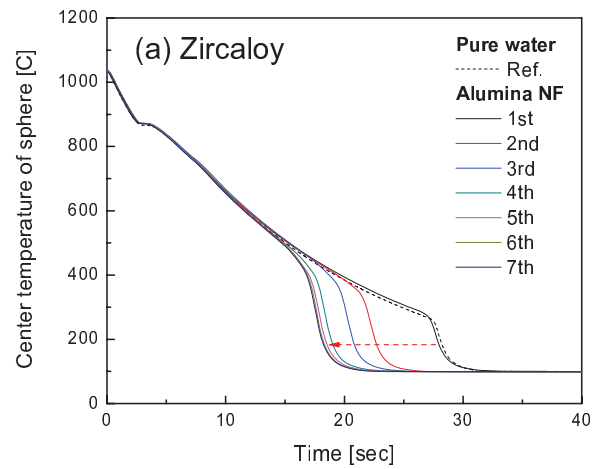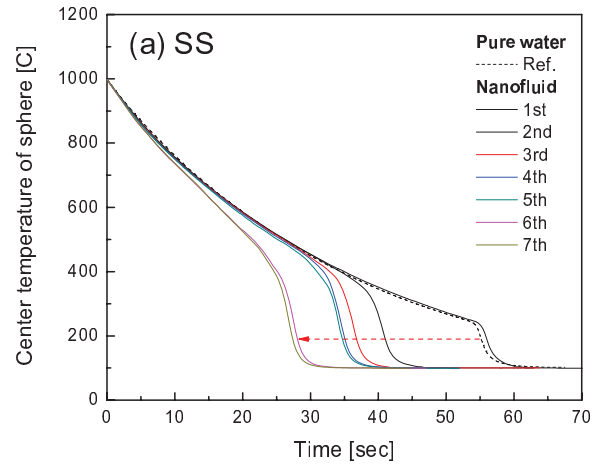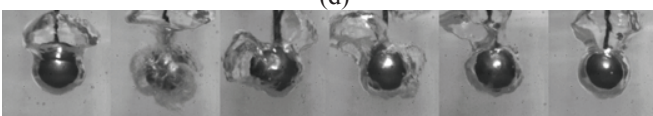
Figure 35 Quenching curves for SS and Zry spheres in 0.1 vol% (a) alumina, (b) silica, and (c) diamond nanofluids at saturated conditions.

3.2.4. Conclusions

The main findings of this study are as follows:

- Film boiling heat transfer in nanofluids is almost identical to that in pure water. That is, the nanoparticles present in the nanofluids have no major effect on the quenching process.

- However, some nanoparticles deposit on the sphere surface during the quenching process, and in *subsequent* quenching tests they can greatly accelerate the end of film boiling, i.e., MHF occurs at a higher wall superheat (by up to 150°C) than on a fresh sphere. The physical mechanism responsible for such acceleration is likely the destabilization of the vapor film, due to the particle deposits on the surface.

CONCLUSIONS

More detailed conclusions can be found in the conclusion sections of the Thermal Conductivity, Convection, and Boiling sections. In summary:

- The thermal conductivity of the nanofluids investigated here followed the behavior predicted by existing models.

- The convection and pressure drop behavior of single phase nanofluids investigated here follow the behavior of existing models.

- For the nanofluids investigated here, boiling of nanofluids shows the most interesting results and promise. Low concentrations of nanofluids can result in a significant enhancement of the critical heat flux and quenching kinetics, but a reduction in the nucleate boiling heat transfers coefficient. It has been shown that existing models can explain these trends.

REFERENCES

[1] J.A. Eastman, Phillpot S. R., Choi S.U.S., Keblinski P., Annu. Rev. Mat. Res., 34, 219-246 (2004).
[2] K. Das, Choi S.U.S., Patel H. E., Heat Transfer Engineering, v 27, n 10, p 3-19 (2006).
[3] S. Kabelac, and J. F. Kuhnke, Annals of the Assembly for International Heat Transfer Conference, 13, KN-11 (2006).
[4] V. Trisaksri, Wongwises S., Renewable and Sustainable Energy Reviews, v 11, n 3, p 512-523 (2007).
[5] X. Q. Wang, A. S. Mujumdar, Int. J. Thermal Sciences, v 46, n 1, p 1-19 (2007).
[6] S. M. S. Murshed, Leong, K.C.; Yang, C., Appl. Thermal Engineering, v 28, n 17-18, p 2109-2125 (2008).
[7] W. Yu, France D. M., Routbort J. L., Choi, S. U. S., Heat Transfer Engineering, v 29, n 5, p 432-460 (2008).
[8] S. K. Das, Choi, S. U. S., Yu, W., Pradeep, T., Nanofluids: Science and Technology, John Wiley & Sons, Inc (2008).
[9] J. Buongiorno, D. Venerus, N. Prabhat, T. McKrell, et al, Journal of Applied Physics, Volume 106, Issue 9, p 094312-094312-14 (2009).
[10] U. Rea, T. McKrell, L. Hu, and J. Buongiorno, International Journal of Heat and Mass Transfer, Volume 52, Issues 7-8, March 2009, p 2042-2048.
[11] W. Williams, J. Buongiorno, and L. Hu, J. Heat Transfer, Volume 130, Issue 4, 042407 (7 pages), (2008).
[12] S. Kim, I. Bang, J. Buongiorno, and L. Hu, International Journal of Heat and Mass Transfer, v 50, Issues 19-20, p. 4105-4116, (2007).
[13] S. Kim, T. McKrell, J. Buongiorno, and L. Hu, J. Heat Transfer, v 131, Issue 4, p 043204, (2009).
[14] H. Kim, G. DeWitt, T. McKrell, J. Buongiorno, and L. Hu, International Journal of Multiphase Flow, v 35, Issue 5, p. 427-438, (2009).
[15] J. C. Maxwell, A Treatise on Electricity and Magnetism, II Edition, Clarendon, Oxford (1881).
[16] Q. Li, and Xuan, Y.M., in Heat Transfer Science and Technology, edited by Buxan Wang, Higher Education Press, pp. 757–762 (2000).
[17] J. A. Eastman, S. U. S. Choi, S. Li, W. Yu, L. J. Thompson, Appl. Phys. Lett., 78(6), 718-720 (2001).
[18] H. U. Kang, S.H. Kim, and J.M. Oh, Experimental Heat Transfer, 19(3), 181-191 (2006).
[19] T.-K. Hong, Yang H., Choi C. J., J. Appl. Phys., 97, 064311 (2005).
[20] S. Jana, A. Salehi-Khojin, W. H. Zhong, Thermochimica Acta, 462, 45–55 (2007).
[21] M. Chopkar, Das P.K., Manna I., Scripta Materialia 55, 549-552 (2006).
[22] S. Shaikh, K. Lafdi, R. Ponnappan, J. Appl. Phys., 101, 064302 (2007).
[23] H. Xie, Wang J., Xi T., and Ai F., J. Appl. Phys., 91, 4568–4572 (2002).
[24] H. Xie, Wang J., Xi T., and Liu Y., Int. J. Thermophysics, 23, 571–580 (2002).
[25] S. M. S. Murshed, Leong K. C., and Yang C., Int. J. Thermal Sciences, 44, 367–373 (2005).
[26] C. H. Chon, K.D. Kihm, S.P. Lee, S.U.S. Choi, Appl. Phys. Lett. 87 153107 (2005).
[27] K. S. Hong, T.-K. Hong, H.-S. Yang, Appl. Phys. Lett. 88 031901 (2006).
[28] S. H. Kim, S. R. Choi, D. Kim, J. Heat Transfer 129 298-307 (2007).
[29] C. H. Li and G.P. Peterson, J. Appl. Phys. 101 044312 (2007).
[30] P. D. Shima, J. Philip, B. Raj, Appl. Phys. Lett., 94, 1 (2009).
[31] S. K. Das, et al., J. Heat Transfer, 125, p. 567 – 574 (2003).
[32] D. Wen, and Ding Y., J. Thermophysics and Heat Transfer, 18, 481–485 (2004).
[33] C. H. Li and G. P. Peterson, J. Appl. Phys., 99, 084314 (2006).
[34] H. D. Kumar, Patel H. E., Rajeev K. V. R., Sundararajan T., Pradeep T. and Das S. K., Phys. Rev. Lett., 93 (14), 144301 (2004).
[35] S. P. Jang and Choi, S. U. S., Appl. Phys. Lett., 84, 4316 (2004).
[36] R. Prasher, Bhattacharya P., and Phelan P. E., Phys. Rev. Lett. 94, 025901 (2005).
[37] H. E. Patel, Sundararajan T., Pradeep T., Dasgupta A., Dasgupta N. and Das S. K., Pramana – J. Physics, 65 (5), 863 – 869 (2005).

[38] H. E. Patel, T. Sundararajan and S. K. Das, J. Nanoparticle Research, Vol 10(1), 87-97 (2008).

[39] P. Keblinski, S. R. Phillpot, S. U. S. Choi, J. A. Eastman, Int. J. Heat Mass Transfer, 45, 855-863 (2002).

[40] B. X. Wang, Zhou, L. P, and Peng X. F., Int. J. Heat Mass Transfer, 46, 2665-2672 (2003).

[41] M. Foygel, Morris R. D., Anez D., French S., and Sobolev V. L., Phys. Rev. B, 71, 104201 (2005).

[42] R. Prasher, W. Evans, P. Meakin, J. Fish, P. Phelan, P. Keblinski, App. Phys. Lett., 89, 143119, (2006).

[43] J. Eapen, J. Li and S. Yip, Phys. Rev. E 76, 062501 (2007).

[44] J. Philip, P. D. Shima and R. Baldev, Nanotechnology, 19, 305706 (7pp) (2008).

[45] W. Yu and S. U. S. Choi, J. Nanoparticle Res., 5, 167 (2003).

[46] J. Eapen, J. Li, and S. Yip, Phys. Rev. Lett. 98, 028302 (2007).

[47] C. W. Nan, R. Birringer, David R. Clarke, H. Gleiter, J. Appl. Phys. 81 (10), 15 May (1997).

[48] P. Keblinski, R. Prasher, J. Eapen, J. Nanoparticle Research, 10, 1089 (2008).

[49] O. M. Wilson, Hu X., Cahill D. G., Braun P. V., Phys. Rev. B, 66, 224301 (2002).

[50] S. Huxtable, Cahill D. G., Shenogin S., Xue L., Ozisik R., Barone P., Usrey M., Strano M. S., Siddons G., Shim M., Keblinski P., Nat. Mater., 2, 731 (2003).

[51] E. V. Timofeeva, A. N. Gavrilov, J. M. McCloskey, Y. V. Tolmachev, S. Sprunt, L. M. Lopatina and J. V. Selinger, Phys. Rev. E., 76, 061203 (2007).

[52] B. C. Pak and Y. I. Cho, Hydrodynamic and heat transfer study of dispersed fluids with submicron metallic oxide particles, Experimental Heat Transfer, 11, 151 (1998).

[53] Y. Xuan and Q. Li. Investigation on convective heat transfer and flow features of nanofluids, Journal of Heat Transfer, 125,151–155 (2003).

[54] Y. Xuan and W. Roetzel, Conceptions for heat transfer correlation of nanofluids. International Journal of Heat and Mass Transfer, 43, 3701–3707 (2000).

[55] Y. Yang, Z. G. Zhang, E. A. Grulke, W. B. Anderson, G. Wu, Heat transfer properties of nanoparticle-in-fluid dispersions (nanofluids) in laminar flow, International Journal of Heat and Mass Transfer, 48, 1107-1116 (2005).

[56] D. Wen and Y. Ding, Experimental investigation into convective heat transfer of nanofluids at the entrance region under laminar flow conditions, International Journal of Heat and Mass Transfer, 47, 5181–5188 (2004).

[57] Y. Ding, H. Alias, D. Wen and R.A. Williams, Heat transfer of aqueous suspensions of carbon nanotubes (CNT nanofluids), Int. J. Heat Mass Transfer, 49, 240-250 (2006).

[58] S. Z. Heris, M. N. Esfahany, and G. Etemad, Investigation of CuO/water nanofluid laminar convective heat transfer through a circular tube, J. Enhanced. Heat Transfer, 13, 279-289 (2006).

[59] S.Z. Heris, M.N. Esfahany, and S. Gh. Etemad, Experimental Investigation of convective heat transfer of Al2O3/water nanofluid in circular tube, Int. J. Heat Fluid Flow, 28, 203-210 (2007).

[60] Y. He, Y. Jin, H. Chen, Y. Ding, D. Chang and H. Lu, Heat transfer and flow behaviour of aqueous suspensions of TiO2 nanoparticles (nanofluids) flowing upward through a vertical pipe, Int. J. Heat Mass Transfer, 50, 2272-2281 (2007).

[61] J. Lee, R.D. Flynn, K.E. Goodson, J.K. Eaton, Convective heat transfer of nanofluids (DI Water-Al2O3) in microchannels, HT2007-32630, ASME-JSME Thermal Engineering Summer Heat Transfer Conference, July 8-12, Vancouver, BC, Canada (2007).

[62] R. Chein and J. Chuang, Experimental microchannel heat sink performance studies using nanofluids, Int. J. Thermal Sci., 46, 57-66 (2007).

[63] C. T. Nguyen, G. Roy, C. Gauthier, and N. Galanis, N., Heat transfer enhancement using Al2O3-water nanofluid for an electronic liquid cooling system, Appl. Thermal Eng., 27, 1501-1506 (2007).

[64] W. C. Williams, Experimental and Theoretical Investigation of Transport Phenomena in Nanoparticle Colloids (Nanofluids), Ph.D. Thesis, Massachusetts Institute of Technology, Cambridge, Feb. 2007.

[65] R. Rusconi, W. C. Williams, J. Buongiorno, R. Piazza and L.W. Hu, Numerical Analysis of Convective Instabilities in a Transient Short-Hot-Wire Setup for Measurement of Liquid Thermal Conductivity, International Journal of Thermophysics, V 28, 4, p. 1131-1146, (2007).

[66] J. H Lienhard IV and J. H. Lienhard V, A heat transfer textbook, 3rd edition, Phlogiston Press (2002).

[67] W. C. Williams, J. Buongiorno, L. W. Hu. The Efficacy of Nanofluids as Convective Heat Transfer Enhancing Coolants for Nuclear Reactor Applications. Proceedings of the 2007 ANS Meeting, Boston, June 24-28, 2007.

[68] B. C. Pak and Y. I. Cho. Hydrodynamic and heat transfer study of dispersed fluids with submicron metallic oxide particles. Experimental Heat Transfer, 11(2):151, (1998).

[69] S. M. You, J. Kim, K. H. Kim, 2003, "Effect of nanoparticles on critical heat flux of water in pool boiling heat transfer", Applied Physics Letters, 83, 16, 3374-3376.

[70] S. Das, N. Putra, W. Roetzel, 2003, "Pool boiling characteristics of nano-fluids", Int. J. of Heat and Mass Transfer, 46, 851-862.

[71] P. Vassallo, R. Kumar, S. D'Amico, 2004, "Pool boiling heat transfer experiments in silica-water nano-fluids", Int. J. of Heat and Mass Transfer, 47, 407-411.

[72] T. N. Dinh, J. P. Thu, T. G. Theofanous, 2004, "Burnout in high heat flux boiling: the hydrodynamic and physico-chemical factors", 42nd AIAA Aerospace Sciences Meeting and Exhibit, Reno, Nevada, 5-6 January.

[73] J. H. Kim, K. H. Kim, S. M. You, 2004, "Pool Boiling Heat Transfer in Saturated Nanofluids", Proceedings of IMECE 2004, Anaheim, California, November 13-19.

[74] G. Moreno Jr., S. Oldenburg, S. M. You, J. H. Kim, 2005, "Pool Boiling Heat Transfer of Alumina-Water, Zinc Oxide-Water and Alumina-Water Ethylene Glycol Nanofluids", Proceedings of HT2005, July 17-22, San Francisco, California, USA.

[75] I. C. Bang and S. H. Chang, 2005, "Boiling Heat Transfer Performance and Phenomena of Al2O3-Water Nano-fluids

from a Plain Surface in a Pool", Int. J. of Heat and Mass Transfer, 48, 2407-2419.

[76] D. Milanova and R. Kumar, 2005, "Role of ions in pool boiling heat transfer of pure and silica nanofluids", Applied Physics Letters, 87, 233107.

[77] D. Wen and Y. Ding, 2005, "Experimental investigation into the pool boiling heat transfer of aqueous based γ-alumina nanofluids", Journal of Nanoparticle Research, 7:265-274.

[78] H. Kim, J. Kim, M. Kim, 2006, "Experimental study on the characteristics and mechanism of pool boiling CHF enhancement using nano-fluids", ECI International Conference on Boiling Heat Transfer, Spoleto, 7-12 May.

[79] H. Kim, J. Kim, M. Kim, 2006, "Experimental study on CHF characteristics of water-TiO2 nano-fluids", Nuclear Engineering and Technology, Vol. 38, No. 1.

[80] D. Milanova, R. Kumar, S. Kuchibhatla, S. Seal, 2006, "Heat transfer behavior of oxide nanoparticles in pool boiling experiment", Proc. of 4th International Conference on Nanochannels, Microchannels and Minichannels, Limerick, Ireland, June 19-21.

[81] C. Gerardi, J. Buongiorno, L. Hu, and T. McKrell, "Infrared thermometry study of nanofluid pool boiling phenomena," Submitted April 9, 2010 to HKIE Outstanding Paper Award for Young Engineers/Researchers 2010.

[82] C. Gerardi, J. Buongiorno, L. W. Hu, T. Mckrell, "Study of Bubble Growth in Water Pool Boiling Through Synchronized, Infrared Thermometry and High-Speed Video," Int. J. Heat Mass Transfer (submitted, 2010).

[83] C. Gerardi, "Investigation of the Pool Boiling Heat Transfer Enhancement of Nano-Engineered Fluids by means of High-Speed Infrared Thermography," PhD Thesis, Massachusetts Institute of Technology (2009).

[84] S.J. Kim, I. C. Bang, J. Buongiorno, L. W. Hu, "Surface Wettability Change during Pool Boiling of Nanofluids and its effect on Critical Heat Flux", Int. J. Heat Mass Transfer, 50, 4105-4116, (2007).

[85] B. Truong, L. W. Hu, J. Buongiorno, T. McKrell, "Modification of Sandblasted Plate Heaters Using Nanofluids to Enhance Pool Boiling Critical Heat Flux", Int. J. Heat Mass Transfer, 53, 85–94, (2010).

[86] B. Truong, "Determination of pool boiling critical heat flux enhancement in nanofluids," B.S. Thesis, Massachusetts Institute of Technology, Cambridge MA USA, May (2007).

[87] S.J. Kim, "Subcooled flow boiling heat transfer and critical heat flux in water based nanofluids at low pressure," Ph.D. Thesis, Massachusetts Institute of Technology, Cambridge MA USA, March (2009).

[88] T.G. Theofanous, J.P. Tu, A.T. Dinh and T.N. Dinh, "The Boiling Crisis Phenomenon", J. Experimental Thermal Fluid Science, 26 (6-7), P.I:pp. 775-792, P.II: pp. 793-810, (2002).

[89] H.D. Kim, M.H. Kim, "Effect of nanoparticle deposition on capillary wicking that influences the critical heat flux in nanofluids," Appl. Phys. Let., 91(1), 014104-1, (2007).

[90] J. Eapen, R. Rusconi, R. Piazza, and S. Yip, "The classical nature of thermal conduction in nanofluids," J. Heat Transfer, (2009)

[91] N. Kurul, M.Z. Podowski, "Multidimensional effects in forced convection subcooled boiling", Proc. 9th International Heat Transfer Conference, Jerusalem, Israel. pp. 21-25, (1990).

[92] R.W. Bowring, "Physical model based on bubble detachment and calculation of steam voidage in the subcooled region of a heated channel," OECD Halden Reactor Project Report HPR-10, (1962).

[93] V.P. Carey, Liquid-Vapor Phase-Change Phenomena (2nd edition), Taylor & Francis Group, New York, (2008).

[94] C.H. Wang, V.K. Dhir, "Effect of surface wettability on active nucleation site density during pool boiling of water on a vertical surface," ASME Journal of Heat Transfer, 115, pp 659-669, (1993).

[95] N. Zuber, "On the stability of boiling heat transfer," Trans. ASME J. Heat Transfer, 8 (3), pp. 711-720, (1958).

[96] T.G. Theofanous, J.P. Tu, A.T. Dinh and T.N. Dinh, "The Boiling Crisis Phenomenon", J. Experimental Thermal Fluid Science, 26 (6-7), P.I:pp. 775-792, P.II: pp. 793-810, (2002).

[97] Y. Haramura, Y. Katto, "A new hydrodynamic model of CHF applicable widely to both pool and forced convection boiling on submerged bodies in saturated liquids," Int. J. Heat Mass Transfer, 26, 389–399, (1983).

[98] P. Sadasivan, P.R. Chappidi, C. Unal, R.A. Nelson, "Possible mechanisms of macrolayer formation," Pool External Flow Boil. (ASME 1992) 135, (1992).

[99] S.G. Kandlikar, "A theoretical model to predict pool boiling CHF incorporating effects of contact angle and orientation," J. Heat transfer, 123, pp. 1071-1079, December (2001).

[100] T.G. Theofanous, T.N. Dinh, High heat flux boiling and burnout as microphysical phenomena: mounting evidence and opportunities, Multiphase Sci. Technol., 18(1), 1–26, (2006).

[101] W. Rosenhow, P. Griffith, "Correlation of maximum heat flux data for boiling of saturated liquids," Chem. Eng. Prog. Symp. Ser. 52 (18), 47–49, (1956).

[102] N.I. Kolev, Multiphase Flow Dynamics 2: Mechanical and thermal interactions, Springer-Verlag, New York, (2002).

[103] N.I. Kolev, "To the nucleate boiling theory," Nucl. Engr. Design., 239(1), pp. 187-192, (2009)